ORGANIC DONOR-ACCEPTOR CHROMOPHORE-CATALYST ASSEMBLY FOR SOLAR FUELS

A Thesis
Presented to
The Academic Faculty

by

Joshua Stuart Hollett

In Partial Fulfillment
of the Requirements for the Degree
Master of Science in the
School of Chemistry and Biochemistry

Georgia Institute of Technology
May 2015

ORGANIC DONOR-ACCEPTOR CHROMOPHORE-CATALYST ASSEMBLY FOR SOLAR FUELS

Approved by:

Dr. John R. Reynolds, Advisor
School of Chemistry and Biochemistry
Georgia Institute of Technology

Dr. Stefan France
School of Chemistry and Biochemistry
Georgia Institute of Technology

Dr. Jake D. Soper
School of Chemistry and Biochemistry
Georgia Institute of Technology

Date Approved: January 9, 2015

To my wife Micaela and our loving, supportive families

ACKNOWLEDGEMENTS

I wish to thank my advisor, Dr. John R. Reynolds, for accepting me into his group and providing me with invaluable wisdom and guidance. Dr. Toan V. Pho was instrumental to my development both in and out of the laboratory and for that I thank him. Many members of the Reynolds group contributed their knowledge and expertise on many occasions and for that I thank them all: James Ponder, Rylan Wolfe, Jeffrey Hernandez, Justin Kerszulis, Natasha Teran, Coralie Richard, Kin Lo, Caroline Grand, Bryan Schmatz, Dylan Christiansen, Ray Bulloch, Anna Österholm, Eric Shen, and Aubrey Dyer.

TABLE OF CONTENTS

LIST OF FIGURES

Page

LIST OF SCHEMES

LIST OF SYMBOLS AND ABBREVIATIONS

A	Amp(s)
ACN	Acetonitrile
bpm	2,2'-bipyrimidine
bpy	2,2'-bipyridine
°C	Degree(s) Celsius
cat.	Catalyst
CB	Conduction band
$CDCl_3$	Deuterated chloroform
$CHCl_3$	Chloroform
chrom.	Chromophore
cm	Centimeter(s)
cm^2	Square centimeter(s)
δ	Chemical shift in ppm
DCM	Dichloromethane
DI	Deionized
d	Doublet
dd	Doublet of doublets
dt	Doublet of triplets
DSPEC	Dye sensitized photoelectrosynthesis cell(s)
DSSC	Dye sensitized solar cell(s)
e^-	Electron
E	Electric potential
ε	Molar extinction coefficient

E_{HOMO}	Highest occupied molecular orbital energy level
E_{LUMO}	Lowest occupied molecular orbital energy level
E_{ox}	Oxidation potential
E_{red}	Reduction potential
ΔE^{opt}	Optical gap
ESI	Electrospray ionization
ET	Electron transfer
eV	Electron volt(s)
equiv.	Equivalent(s)
Fc	Ferrocene
FF	Fill factor
FPT	Freeze-pump-thaw
g	Gram(s)
h^+	Hole
^1H NMR	Proton nuclear magnetic resonance
HOTf	Triflic acid
HOMO	Highest occupied molecular orbital
I_{max}	Maximum current
IPCE	Incident photon-to-current efficiency
J_{SC}	Short circuit current
LUMO	Lowest occupied molecular orbital
M	Molar
$[M]^+$	Molecular ion
mA	Milliamp(s)
MALDI-TOF	Matrix-assisted laser desorption/ionization – time of flight

Mebim-py	2,6-bis(1- methylbenzimidazol-2-yl)pyridine)
MeOH	Methanol
MHz	Megahertz
mi^2	Square mile(s)
min	Minute(s)
mL	Milliliter(s)
mM	Millimolar
mmol	Millimole(s)
MS	Mass spectrometry
mV	Millivolt(s)
m/z	Mass-to-charge ratio
NBS	*N*-bromosuccinimide
NHE	Normal hydrogen electrode
nm	Nanometer(s)
OD	Oven dried for at least 24 hours at 130 °C
OEC	Oxygen evolving complex
PCE	Power conversion efficiency
PCET	Proton coupled electron transfer
pH	Log of hydrogen ion concentration
ppm	Part(s) per million
ps	Picosecond(s)
psi	Pound(s) per square inch
PSII	Photosystem II
PTLC	Preparative thin layer chromatography
q	Quartet

r.f.	Retention factor
r.t.	Room temperature
s	Second(s)
SCE	Saturated calomel electrode
SPS	Solvent purification system
t	Time
THF	Tetrahydrofuran
TLC	Thin layer chromatography
TN	Turnover number
TW	Terawatt(s)
tpy	2,2’ :6’,2’’-terpyridine
UV	Ultraviolet
UV-Vis	Ultraviolet-visible
V	Volt
V_{OC}	Open circuit voltage
VB	Valence band
W	Watt
WOC	Water oxidation catalyst

SUMMARY

In this thesis, a novel chromophore-catalyst molecular assembly is synthesized in the pursuit of affecting rapid water oxidation driven by light. The compound is inspired by previous work done in the lab of John R. Reynolds by Toan V. Pho in making a covalently attached all donor organic chromophore-catalyst assembly; as well as, the work of Thomas J. Meyer in utilizing covalently attached inorganic chromophore-catalyst assemblies based on ruthenium. The impact of the thesis work revolves around the broader ultraviolet-visible (UV-Vis) profile of the conjugated donor-acceptor chromophore described herein coupled with the promising current generating insights of a similar chromophore previously synthesized by Romain Stalder, in the Reynolds group, for use in dye sensitized solar cells (DSSCs).[1] The photocurrent response and water oxidation experiments remain to be completed, and will be done by collaborators at the University of North Carolina Chapel Hill.

CHAPTER 1

INTRODUCTION

1.1 The Current Energy Crisis

The energy supply state of the art is predominantly carbon based fossil fuels. The implications of continuing to rely on fossil fuels are enhanced greenhouse effect, pollution, and decreasing energy stock that will one day fail to support the projected demand.[2] Figure 1.1 starkly captures the global energy challenge that must be met over the next 30 years, in which society must implement widespread use of renewable energies in order to meet the accelerating energy demand forecasted in green. At present, hydrocarbons provide ~85% of the energy in the United States (Figure 1.1 grey curve). [3]

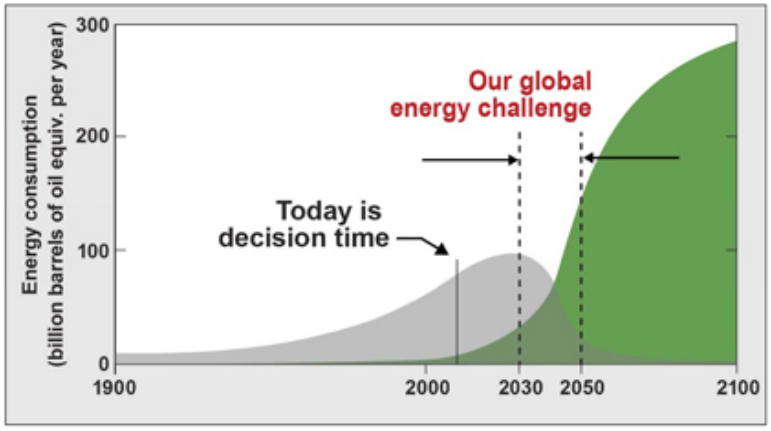

Figure 1.1: Diminishing energy supply (grey) and rapidly accelerating energy demand (green) are producing a window of opportunity for new energy solutions.[4]

The transportation economy relies on oil, but most people believe peak oil will be reached between 2008 and 2025.[3] Therefore, it is time to speedily pursue alternative sources of energy. Renewables that mitigate pollution are most desirable.

1.2 The Need for Renewables

Hydrocarbons will continue to play a major role in the energy sector; however, in order to realize a future with an adequate energy supply and a healthy environment, ecologically benign renewable energy technologies must be implemented.[3] Wind-, bio-, hydroelectric-, solar-, and geothermal energy are some well-known examples of renewables. All of these, with the exception of geothermal energy, come either directly or indirectly from the sun. Heat from the sun gives rise to the wind. Heat and light from the sun cultivates plants whose biomass can be consumed for energy. Heat from the sun evaporates water with subsequent glacial run-off allowing access to hydroelectric energy. Light from the sun is directly converted into electricity or stored in various formats. It is clear then, that the sun will play a major role in the creation of the future energy landscape.[2]

1.3 Old Faithful: The Sun

Italian photochemist Giacomo Caimician exclaimed "…life and civilization will continue as long as the sun shines!"[2] Every hour enough solar radiation reaches the Earth's surface to meet all of its energy demands for a year.[2] In fact, the transformation of sunlight into electricity and fuel is one of the most promising solutions to the world's energy crisis. This energy is pollutant free and is not confined to certain corners of the Earth.[3] In order to meet the current U.S. power demands of 3 terawatts (TW), solar cells of 10% efficiency covering an area the size of North Carolina (~60,000 mi^2) would need to be installed.[3] With energy demands always increasing, more efficient devices are necessary to meet future energy needs. Another hindrance to complete reliance on photovoltaics is the estimated 6 hours of useful sunlight per day worldwide.[3]

1.4 Solar Fuels For When The Sun Goes Down

To power the remaining 18 hours per day, photovoltaics must be paired with energy storage capacities. The advantage of fuels over batteries is that the energy density is between 50 to 100 times greater.[2] To that end, only storage of solar energy in chemical bonds is sufficient for the levels of energy required for those 18 hours.[3] Liquid and gaseous forms of energy are most desirable, as they would utilize the energy infrastructure that already exists (e.g. petroleum and natural gas). Excess solar energy captured during the day could be transformed into hydrogen and hydrocarbons, and utilized by power plants and automobiles at night. The process by which this would occur is analogous to the process of photosynthesis in green plants.[3]

Photosynthesis, a natural scheme for harvesting solar energy, exists in the cells of plants. Scientists have mimicked this scheme and produced several flavors of artificial photosynthesis that utilize the characteristic single electron transfer processes of photo system II (PSII) that store solar energy in chemical bonds. Interested scientists like Björn Akermark contributed to the knowledge of the Mn_4Ca cluster in PSII by synthesizing multi-nuclear manganese mimics.[2] Today, researchers like Daniel Nocera look to low-cost earth abundant metals like cobalt to make artificial photosynthetic devices that even have the ability to self-heal.[2]

Many catalysts have been designed to mimic water oxidation due to an activation energy barrier that induces a limiting overpotential. In 2008, Bernhard and coworkers developed dual site iridium catalysts that evolved oxygen in the presence of water and inspired Brudvig and Crabtree to begin work on single-site iridium catalysts and iridium catalysts co-adsorbed to semiconductors with porphyrin photosensitizers.[2] Iridium metal centers

are synthetically appealing due to their ability to be easily tuned and take on multiple geometries.[2]

The specific technology being considered in this thesis is the ruthenium based dye sensitized photoelectrosynthesis cell (DSPEC).[5] The DSPEC is designed to split H_2O into protons and oxygen and then convert those protons into either hydrogen gas, or hydrocarbons if CO_2 reduction is employed in tandem. It has enormous potential to substitute fossil fuel usage among the various technologies available.

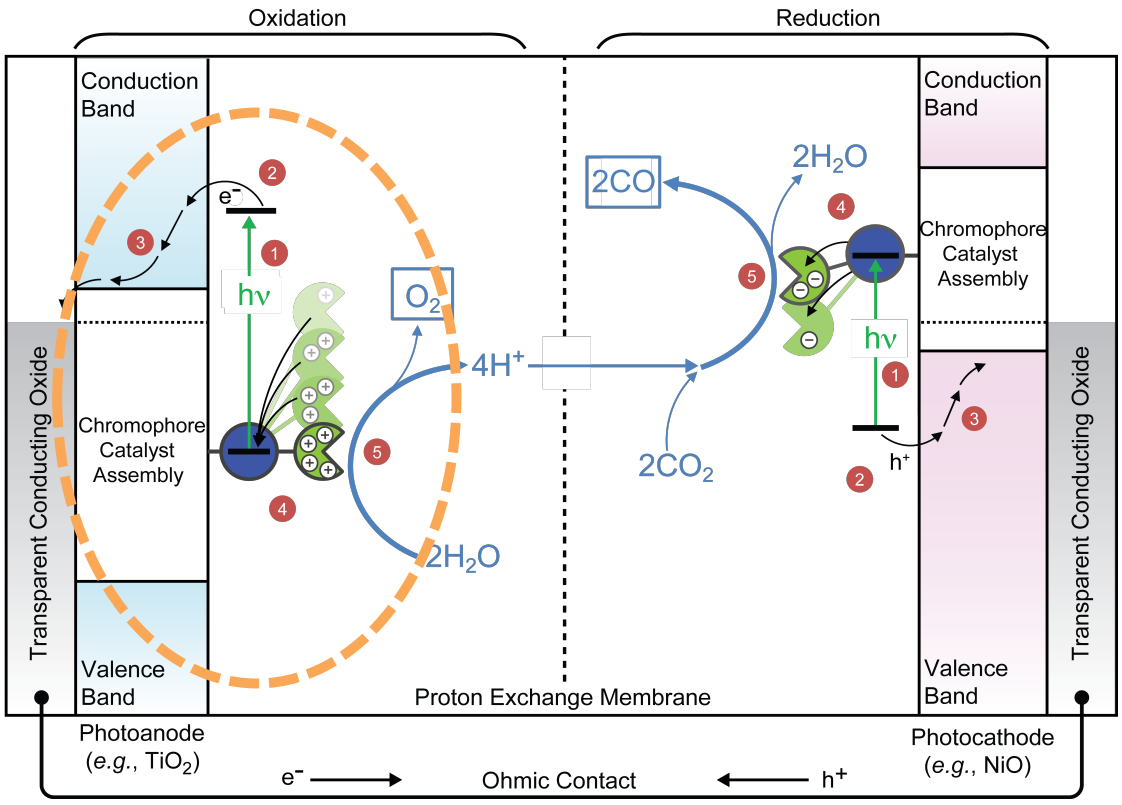

Figure 1.2: DSPEC technology for artificial photosynthesis. Adapted from reference 5.

The DSPEC technology will ideally incorporate both water oxidation, the transformation to the left of the proton exchange membrane, and hydrogen reduction, the transformation to the right of the proton exchange membrane, in one device; however, this thesis and the remainder of this section are concerned only with the processes and components

encircled in orange that involve water oxidation. In Figure 1.2, a blue circle denotes the chromophore and a green Pac-Man-like shape denotes the catalyst of the chromophore-catalyst assembly. Process 1 represents light absorption by the chromophore, which creates an excited state denoted as 2. The electron in the excited state is then injected into the semiconductor in process 3 while the hole is transferred to the covalently attached water oxidation catalyst (WOC) in process 4. Process 5 denotes the transformation of water into protons and oxygen for every four absorption, excitation, injection, and hole transfer processes.

1.4.1 Honda and Fujishima – Water Photolysis

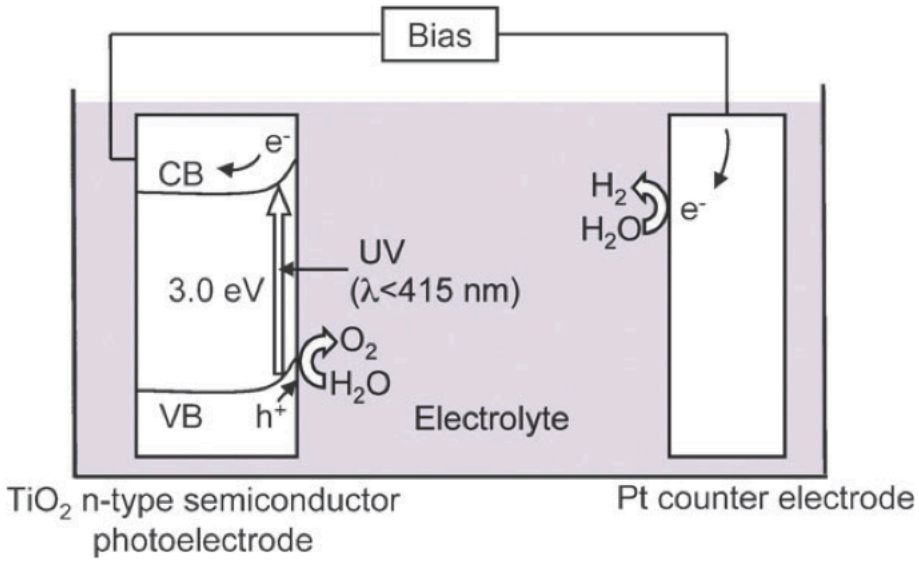

Figure 1.3: Honda-Fujishima effect – water splitting using a TiO_2 photo-electrode.[6]

In 1972, Honda and Fujishima reported the first photocatalytic method of water oxidation.[7] As depicted in Figure 1.3, they irradiated water in the presence of TiO_2 (~ 3.0 eV bandgap) and UV light (≤ 415 nm), and observed the evolution of oxygen gas at -0.5 V (saturated calomel electrode (SCE)) in an aqueous electrolyte of pH 4.7.[7] This was

more negative than the standard water oxidation potential of 0.99 V (SCE) in an aqueous electrolyte at pH 0.[7] The phenomenon was termed "photosensitized electrolytic oxidation." The anodic flow of current indicated that oxygen evolution took place at the anode (TiO_2) and hydrogen evolution took place at the cathode (Pt).[7]

Several semiconductors were tested for their ability to photosensitize[7]; however, it was found that wide band gap semiconductors were needed for stability purposes. Theoretically, semiconductors with ~1000 nm band gaps would be most efficient because the energy needed to oxidize water is only 1.23 V (NHE). Unfortunately, when narrow band gap semiconductors are utilized they corrode.[8] Thomas J. Meyer took a dye-sensitized approach to photosensitization, electing to incorporate inorganic Ru catalysts.

1.4.2 Blue Dimer

In 1978, single site ruthenium catalysts were investigated for their oxidative capabilities but were found not to oxidize water.[9] The oxygen evolving complex (OEC) of PSII comprises a Mn_4Ca cluster bridged by oxygen molecules. However, in 1982, it was thought that the OEC included a Mn dimer.[10] Therefore, in pursuit of an artificial photosynthetic mimic, oxygen bridged ruthenium dimers were pursued. The Meyer group had reported the synthesis of a number of oxygen bridged dimeric ruthenium species in 1975, as they sought to understand the emergence of blue-green colors from bis(bipyridine)ruthenium(II) complexes that were exposed to air over several days.[11]

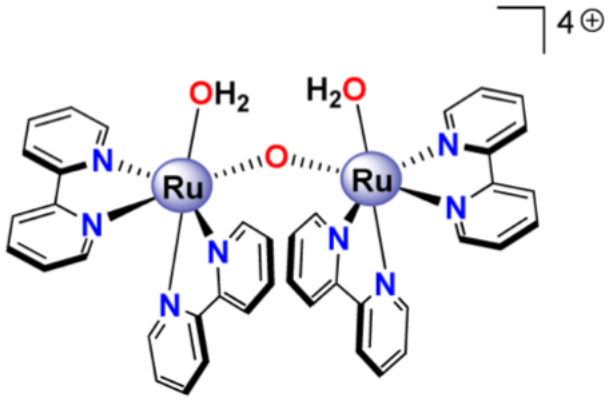

Figure 1.4: Molecular Structure of the blue dimer, *cis,cis*-$[(bpy)_2(H_2O)RuORu(H_2O)(bpy)_2]^{4+}$.[2]

The Meyer group observed strong Ru-O-Ru interactions that markedly changed the chemical and physical properties of the material relative to its monomeric counterparts. Most importantly, in 1982, the blue dimer, shown above in Figure 1.4, affected rapid water oxidation.[10] Unfortunately, the blue dimer was prone to fragmentation, which severely impacted the lifetime of the catalyst.[10] However, the Meyer group was unsure whether or not dimeric or higher order complexes were necessary to realize catalytic water oxidation and continued research on single site ruthenium complexes that began in 1975.[10]

1.4.3 Single Site Ruthenium Catalysts

Single site ruthenium catalysts for oxidation of halides were discovered in 1975, but around that time they were unable to oxidize water. It took ~30 years for the Meyer group to discover that the single sit ruthenium catalysts could produce oxygen and that dimeric species were not necessary. It turns out that graduate student Bruce A. Moyer had solved the problem in 1975; however, he was 100 mV off from the thermodynamic level needed to oxidize water.[12]

In 2005, Thummel demonstrated water oxidation using single site ruthenium catalysts with a maximum turnover number (TN) = 580, where TN is the moles of generated O_2 versus the moles of catalyst.[13] Meyer then reported 100 (±3)% of the expected O_2 after 7.5 turnovers of his Ru-terpyridine(tpy)-bipyrimidine(bpm)$(OH_2)^{2+}$ in 2008. Both reports advanced the field of water oxidation by demonstrating electrolysis of water using simpler catalysts than the dimeric species. The next development was to increase the light sensitization of the complexes in order to affect water oxidation without an applied bias.[12]

1.5 Light Sensitizers Can Help

In principle, water oxidation can be coupled to a light absorption process. The ideal outcome of such an arrangement would be the production of oxygen driven entirely by solar irradiation. A modular approach is best so that each aspect can be studied and then combined to give a working device. The approach would utilize light absorption, electron injection, and intramolecular electron transfer. It would also avoid back electron transfer of injected electrons. The device architecture discussed in this thesis is known as the DSPEC. Theoretically, the chromophores can be either covalently attached to the catalysts or co-adsorbed with the catalysts to the semiconductor surface through binding phosphonate groups. Inorganic Ru chromophores were first used as a result of their electron transfer (ET) and proton-coupled electron transfer (PCET) mechanisms being heavily studied.[14]

1.5.1 Inorganic Ru Chromophores

The Meyer group covalently attached an inorganic Ru chromophore, drawn in blue in Figure 1.5 below, to their Ru(tpy)-bipyridine(bpy) catalyst, drawn in green, and boosted light sensitization as a result of a modest 15,000 $M^{-1}cm^{-1}$ extinction coefficient. More importantly, the assembly demonstrated ultrafast (145 ps) intramolecular hole transfer from chromophore to catalyst.[5]

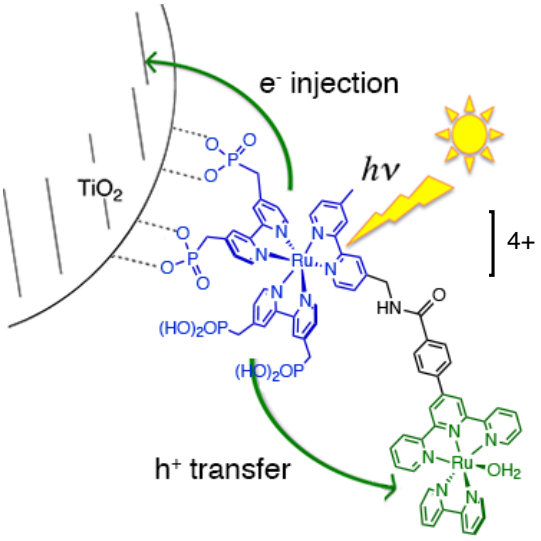

Figure 1.5: Inorganic Ru chromophore-catalyst assembly. Adapted from reference 5.

With respect to organic chromophores, the inorganic Ru chromophore in Figure 1.5 and others like it often have lower molar extinction coefficients,[15] which led to an interest in implementing organic chromophores with the ability to absorb more light. In addition, inorganic Ru chromophores tend to be limited to an absorption range that does not regularly extend beyond 550 nm, into the visible or near-infrared regions.[5, 16] In response to these factors, the Reynolds lab developed a covalently attached organic terthiophene chromophore-catalyst molecular assembly detailed in the following section.

1.5.2 Organic Terthiophene Chromophores

Beyond their higher extinction coefficients, organic chromophores generally offer greater tunability of energy levels and absorption profiles. In order to isolate the effects of increased extinction coefficient as much as possible, the terthiophene chromophore and (tpy)(bpy) based Ru catalyst were covalently attached. Phosphonic acids were placed on the terthiophene chromophore in order to anchor the assembly onto TiO_2. Doing so positions the LUMO as close to the semiconductor as possible to allow for ultrafast femtosecond election injection.

Figure 1.6 shows the HOMO and LUMO energy levels of three potential chromophores inspired by previous work done in the Reynolds group by Romain Stalder,[17] with respect to the oxidation potential of water indicated by the dashed orange line at 1.23 V. The HOMOs of the terthiophene and thiophene-benzothiadiazole-thiophene chromophores are greater than the 1.23 V oxidation potential of water, enabling potential hole transfer from a photooxidized chromophore to a neighboring WOC.

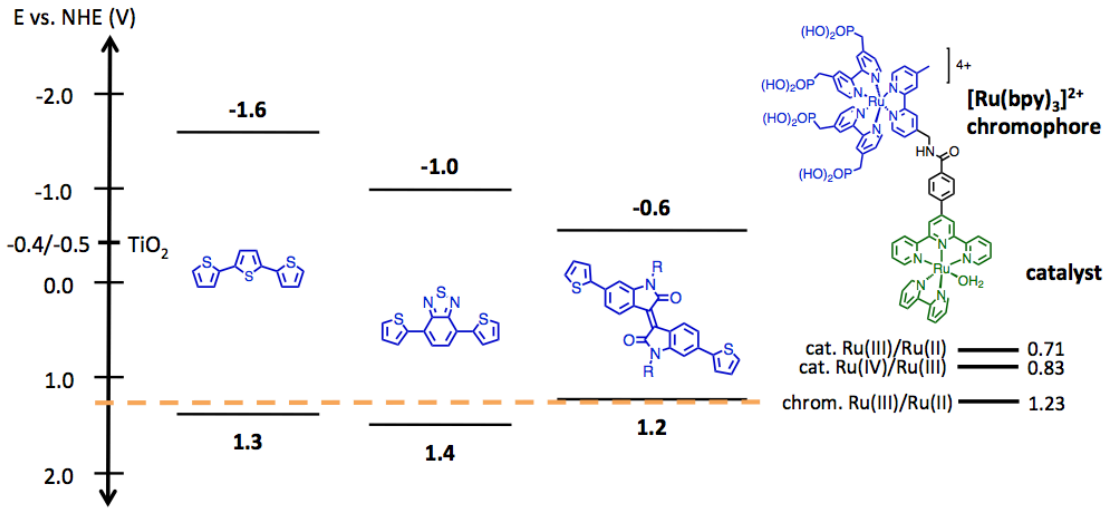

Figure 1.6: Energy level tuning of desirable chromophores (blue) based on the work of Romain Stalder.[17] The dashed orange line shows the oxidation potential of water (1.23 V). Redox potentials of the model assembly from Figure 1.5 are included for reference.

The terthiophene chromophore chosen by Toan V. Pho in the Reynolds lab for the all donor chromophore-catalyst assembly in Scheme 1.1 was inspired by Stalder's **T6-A**[1, 17] seen in Figure 1.7. DSSC data reported by Stalder based on all donor oligothiophene and donor-acceptor moieties displayed in Figures 1.7 and 1.8 indicated promise for similar light absorbers to generate photocurrent in DSPECs. The terthiophene was expected to have a lower extinction coefficient than **T6-A**'s 48,700 $M^{-1}cm^{-1}$ due to containing half the number of thiophene rings in conjugation (3 compared with 6).[17]

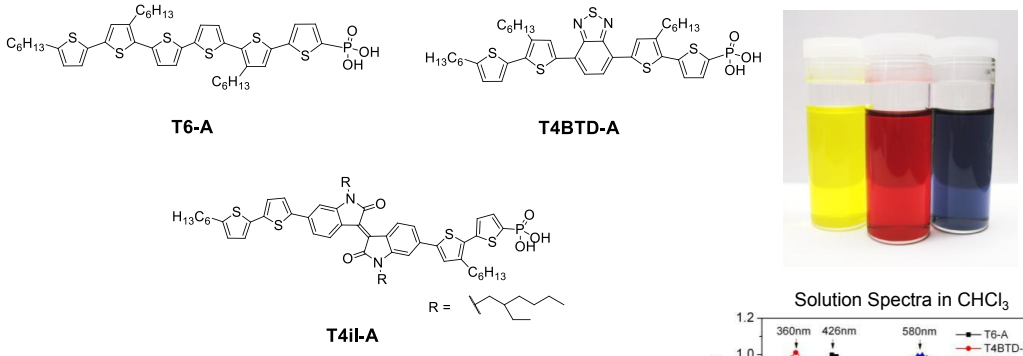

Dye	l_{max} (nm)	ΔE^{opt} (eV)	ε ($M^{-1}cm^{-1}$)	E_{HOMO} (eV)	E_{LUMO} (eV)
T6-A	426	2.40	48700	5.30	2.90
T4BTD-A	508	2.04	21000	5.50	3.55
T4il-A	580	1.77	37500	5.55	3.95

Figure 1.7: Organic chromophores for DSSCs based on the work of Romain Stalder.[17]

In Figure 1.8, devices made with **T6-A** exhibited modest photocurrents of 6.43 mA/cm^2 and device efficiencies of 2.56%.[17] In addition, incident photon-to-current efficiency (IPCE) data at 70% photon-to-current-efficiency indicated good conversion of absorbed light into photocurrent.

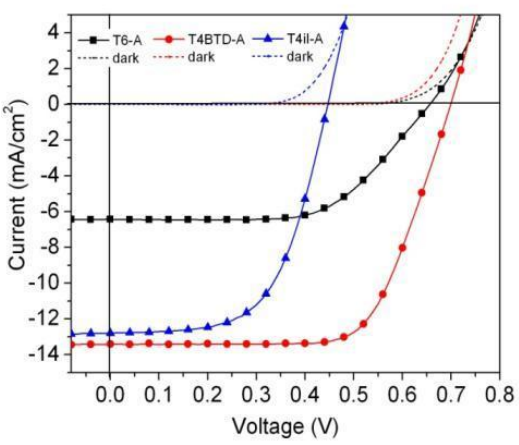

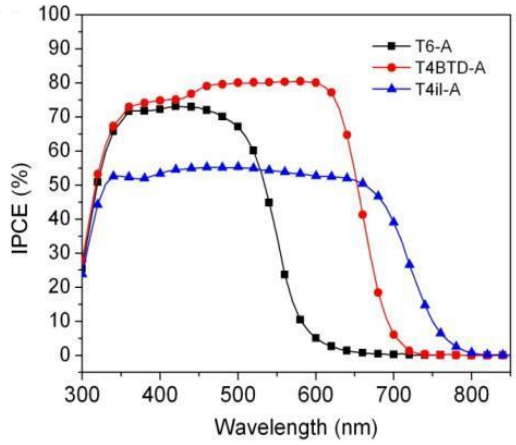

Dye	J_{sc} (mA/cm^2)	V_{oc} (V)	FF (%)	PCE (%)
T6-A	6.43	0.66	61	2.56
T4BTD-A	13.41	0.70	68	6.40
T4il-A	12.79	0.45	59	3.39

Figure 1.8: DSSC characteristics based on the work of Romain Stalder.[17] The accentuation of **T4BTD-A** in orange is to signify the inspiration for the thesis work described in chapter 2.

In Scheme 1.1 the chromophore **1.1** is highlighted in blue and was synthesized primarily though Stille coupling reactions. An extension of the chromophore/one of the catalyst ligands highlighted in green and black was synthesized via a Kröhnke reaction followed by a Stille coupling, before being reacted with **1.1** to yield **1.2** in 64% yield. Compound **1.2** underwent ligand exchange to yield **1.3** in 51% yield, which was subsequently deprotected to **1.4** and on to **1.5** to yield the desired chromophore-catalyst assembly $[Ru(tpy)(bpy)OTf\text{-}T_3\text{-}PO_3H_2]^+$.

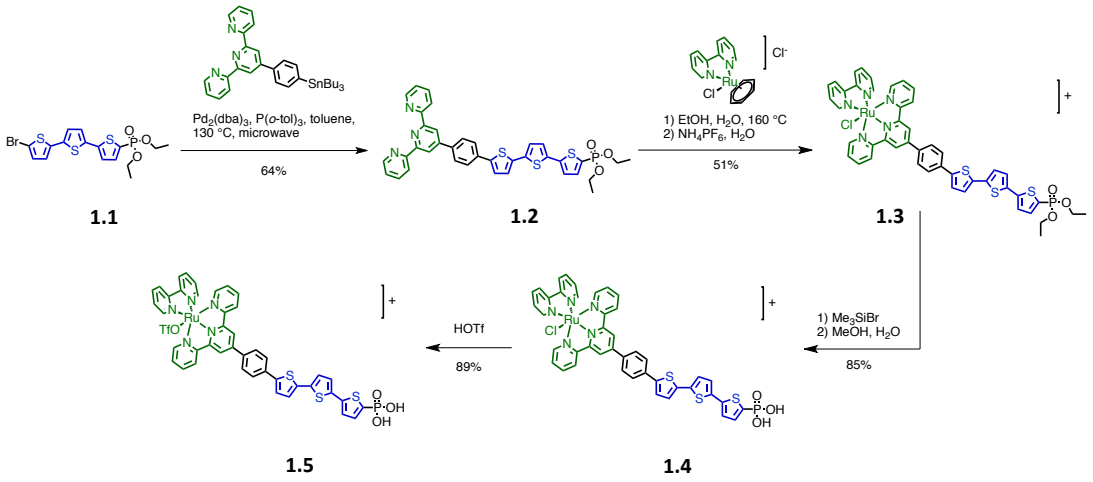

Scheme 1.1: Synthesis of all donor terthiophene chromophore-catalyst assembly **1.5** $[Ru(tpy)(bpy)OTf\text{-}T_3\text{-}PO_3H_2]^+$.

Solution UV-Vis experiments in acetonitrile were conducted on **1.2**, **1.5** (aceto-complex), and a model catalyst to compare light absorbing capabilities and spectral coverage.

Figure 1.9 indicated enhanced optical absorption of terthiophene-catalyst assembly **1.5** relative to the model catalyst. The broad absorption of the assembly suggests electronic communication between the terthiophene chromophore and the Ru(tpy)(bpy) catalyst.

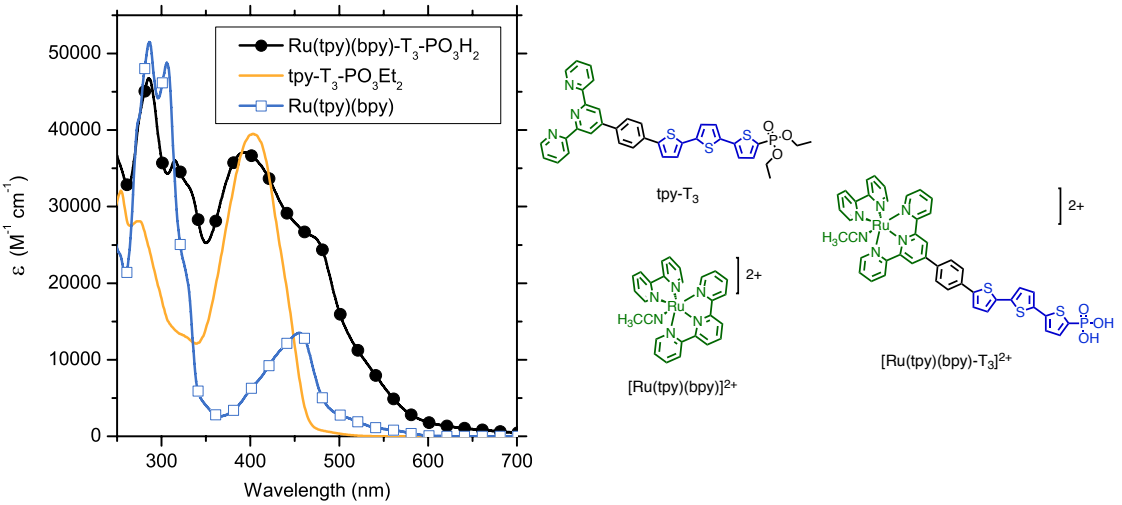

Figure 1.9: Improved light capture and broadening of spectral range of chromophore-catalyst assembly **1.5** (black) relative to model catalyst (blue) and chromophore **1.2** (orange) respectively.

Electrochemical experiments in acetonitrile were conducted on **1.2**, **1.5** (aceto- complex), and a model catalyst to compare redox potentials.

The results reported in Figure 1.10 indicate that the oxidation potential of the catalyst (shown in blue) is unchanged by attachment of the chromophore (shown in orange) in **1.5** (shown in black). Also, the oxidation potential of the chromophore **1.2** and reduction potential of the catalyst were relatively unchanged in the chromophore-catalyst assembly **1.5** (less than a 100 mV difference).

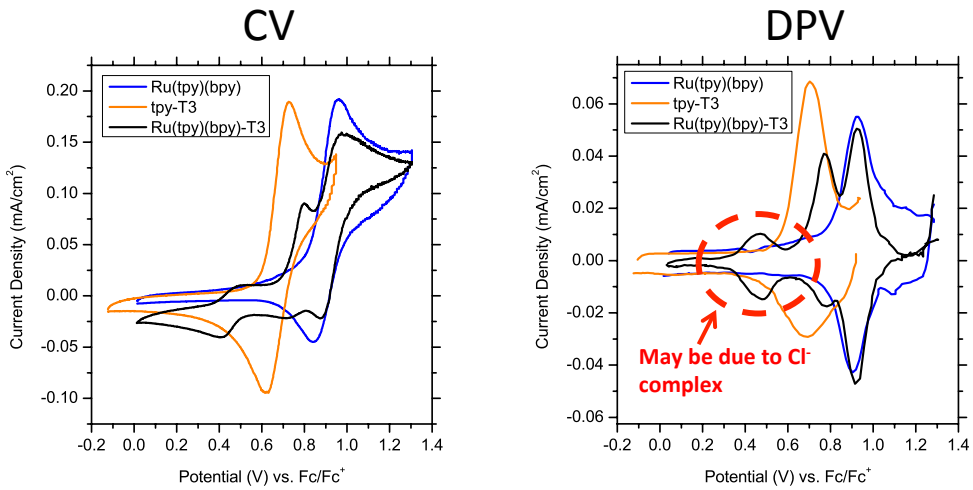

Compound	Ru(tpy)(bpy)	tpy-T3	Ru(tpy)(bpy)-T3
E_{ox}, V	0.90 (0.91)	0.68 (0.69)	0.45, 0.76, 0.93 (0.47, 0.77, 0.92)
E_{red}, V	-1.67 (-1.67)	-- --	-1.60 (-1.61)

Figure 1.10: Electrochemical analysis and energy level determination of model catalyst (blue), chromophore **1.2** (orange), and chromophore-catalyst assembly **1.5** (black). DPV values are given in parentheses.

The final step was to assess the chromophore-catalyst's **1.5** ability to oxidize water. While the oxygen detection experiment remains to be done, an enhancement in photocurrent relative to the Ru(tpy)(Mebim-py) model catalyst would indicate that the chromophore is effective at sensitizing the catalyst.

Figure 1.11 communicates that message exactly, showing the enhanced photocurrent of the terthiophene chromophore-catalyst assembly in blue over the model catalyst in green. In fact, the photocurrents obtained are on par with inorganic chromophore-catalyst assemblies.

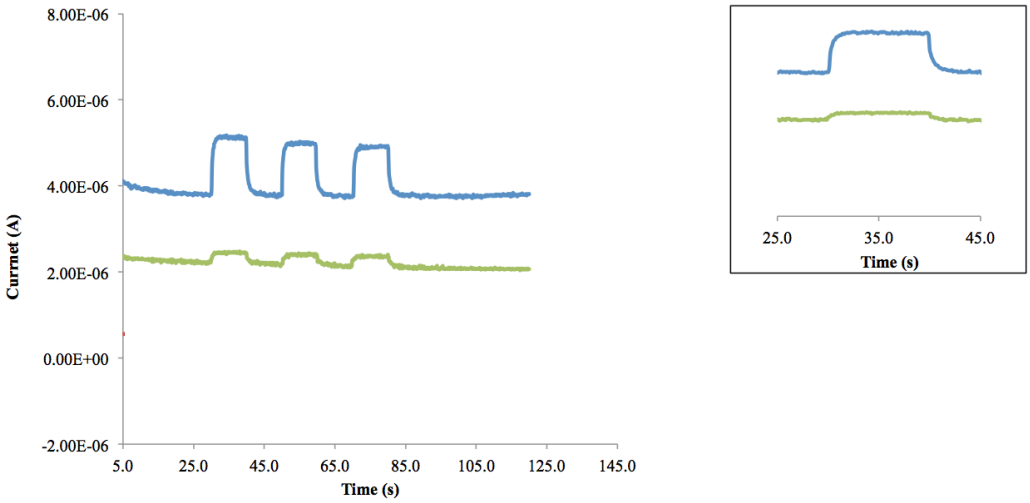

Figure 1.11: Water splitting experiment of chromophore-catalyst assembly **1.5** (blue, aquo-) compared with photocurrent response from Mebim-py model catalyst (green). Experiments were performed in pH 4, 0.5 M $NaClO_4$, 50 mM phosphate buffer solutions with blue 450 nm light. The light was pulsed three times for 10 s each.

Building off of the all donor terthiophene organic chromophore-catalyst assembly work by Toan V. Pho and collaborators at the University of North Carolina Chapel Hill, the next step in the project was to move to donor-acceptor chromophores and covalently attach those to WOCs in order to increase sensitization of the catalysts toward less energetic light. Figure 1.8 indicated a promising two-fold increase in J_{sc} and device efficiency for the donor-acceptor chromophore **T4BTD-A** (accentuated in orange) relative to the all donor **T6-A**. Increases in IPCE and a bathochromic shift of the spectral profile in Figure 1.7 also made a donor-acceptor chromophore-catalyst assembly based off of **T4BTD-A** a natural choice for the thesis work described herein.

CHAPTER 2

ORGANIC DONOR-ACCEPTOR CHROMOPHORE-CATALYST ASSEMBLY FOR WATER OXIDATION

2.1 Terpyridine Chromophore/Catalyst Ligand Synthesis

In this thesis work, the donor-acceptor terpyridine chromophore/catalyst ligand **2.4** (Scheme 2.2) was synthesized in an approach analogous to the all donor terthiophene chromophore/catalyst ligand **1.2** outlined in Scheme 1.1. The colors used to signify the chromophore (blue) and catalyst (green) in the following figures and schemes for the donor-acceptor moieties parallel the colors used for the all donor moieties, except for the incorporation of purple to signify the acceptor unit in the chromophore. In Scheme 2.1, the chromophore **2.2** highlighted in blue/purple was synthesized through Stille coupling reactions. In Scheme 2.2, an extension of the chromophore/one of the catalyst ligands, highlighted in green and black, was synthesized via a Kröhnke reaction followed by a Stille coupling. It was then reacted with **2.3** to yield the donor-acceptor terpyridine chromophore/catalyst ligand **2.4**. All characterization data is discussed in section 2.3 Molecular Characterization.

2.1.1 The T-BTD-T Phosphonate Ester

As seen in Scheme 2.1, the synthesis of **2.1** involved the Stille coupling of 4,7-dibromobenzo[*c*][1,2,5]thiadiazole to diethyl (5-(trimethylstannyl)thiophen-2-yl)phosphonate. The material was chromatographed twice to ensure purity, leading to a

yield of 41%. A Stille coupling of **2.1** with 2-(tributylstannyl)thiophene was conducted in the microwave reactor. The material was chromatographed once leading to **2.2** in a yield of 93%.

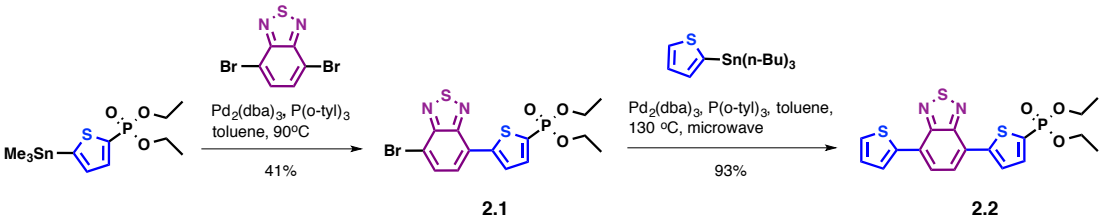

2.1 **2.2**

Scheme 2.1: Synthesis of the T-BTD-T (thiophene-benzothiadiazole-thiophene) phosphonate ester chromophore **2.2**.

With **2.2** in hand, the next step was to connect the terpyridine.

2.1.2 Connecting the Terpyridine

As seen in Scheme 2.2, the synthesis of **2.3** required the bromination of **2.2** with *N*-bromosuccinimide (NBS). The reaction was conducted three times, the final experiment yielding **2.3** in 96% yield without the need for purification. The first two experiments were monitored by thin-layer chromatography (TLC), which proved to be an ineffective method for assessing the course of the reaction. The starting material **2.2** and product **2.3** had identical retention factor (r.f.) values and fluorescent colors. Proton nuclear magnetic resonance spectroscopy (^{1}H NMR) was used in the third experiment to assess the course of the reaction, and nicely indicated complete conversion to **2.3** after 19 hours at reflux.

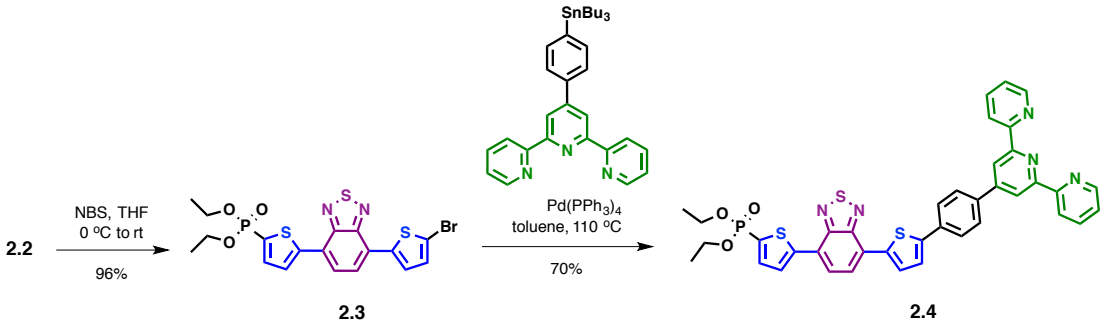

Scheme 2.2: Synthesis of the (tpy)T-BTD-T chromophore/catalyst ligand **2.4**.

In order to capitalize on time, a UV-Vis comparison of T-BTD-T **2.3** against T_3 **1.1** and the model catalyst $[Ru(tpy)(bpy)]^{2+}$ was conducted to compare extinction coefficients and spectral profiles.

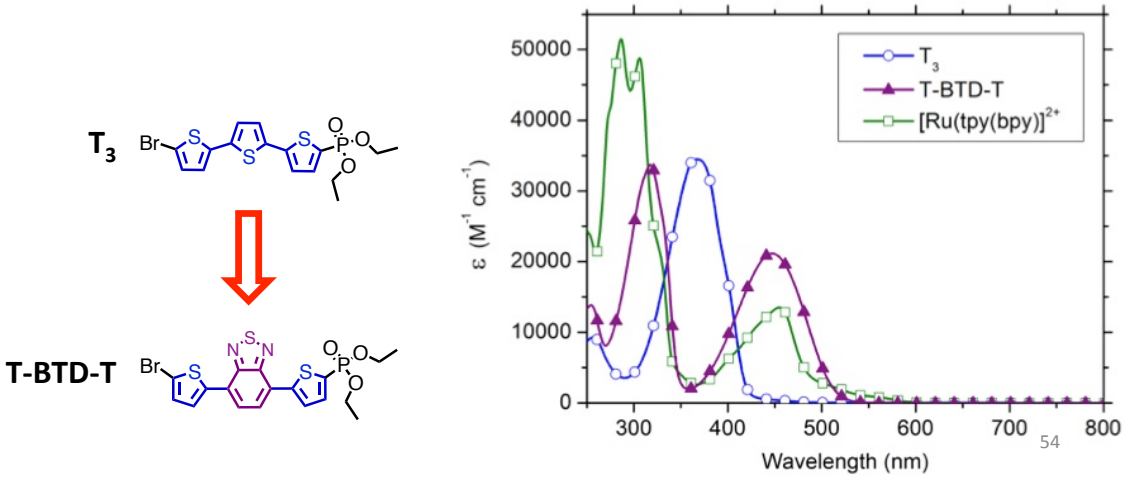

Figure 2.1: Comparison of UV-Vis spectral profiles of T3 **1.1** (blue), T-BTD-T **2.3** (purple), and model catalyst $[Ru(tpy)(bpy)]^{2+}$ (green).

The spectral profiles in Figure 2.1 exhibit the same trend as in Romain Stalder's work seen in Figure 1.7. The donor-acceptor chromophore is red-shifted in relation to the all donor chromophore and the molar extinction coefficient of the longest wavelength λ_{max} is reduced.

The final synthetic hurdle was to assemble the catalyst to the chromophore/catalyst ligand. Synthesis of **2.4** was achieved by Stille coupling of 4'-(4-(tributylstannyl)phenyl)-

2,2':6',2''-terpyridine with **2.3**. The material was chromatographed once followed by 3 consecutive precipitations into hexanes. The precipitations were employed to remove tributyltin junk identified via ^{1}H NMR from the product. The highly polar and non-aliphatic nature of **2.**4 was exploited to affect the purification. The result was the removal of aromatic impurities along with the removal of tributyltin containing impurities as evidenced by ^{1}H NMR, leading to **2.4** in a yield of 70%.

2.2 Attaching the Catalyst

In Scheme 2.3, [Ru(bpy)(η^6-Bz)(Cl)]Cl undergoes ligand exchange with the (tpy)T-BTD-T chromophore/catalyst ligand **2.4** in a microwave reaction adapted from reference 5. Anion exchange with NH_4PF_6 followed by purification via preparative thin-layer chromatography (PTLC) gives the PF_6^- salt **2.5** in a yield of 17%. Compound **2.5** was subsequently deprotected in two steps to afford **2.6** in a yield of 53%.

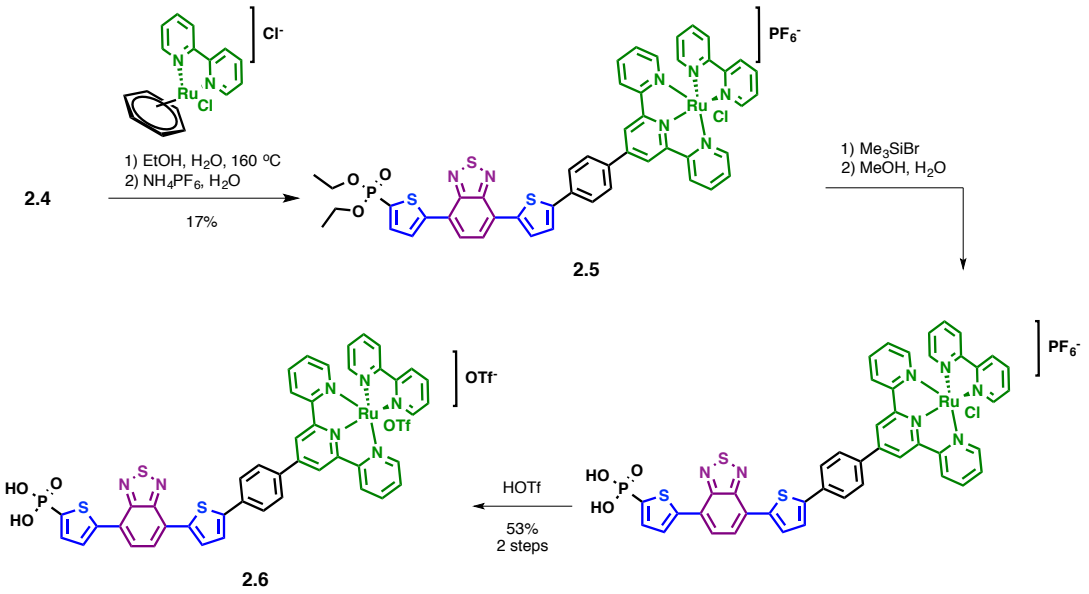

Scheme 2.3: Synthesis of the Ru(OTf)(tpy)(bpy)T-BTD-T phosphonic acid **2.6**.

2.3 Molecular Characterization

The following three sections contain the experimental details, ^{1}H NMR and mass spectrometry (MS) data confirming the successful synthesis of novel compounds **2.1-2.6**.

2.3.1 Experimental

Diethyl (5-(7-bromobenzo[*c*][1,2,5]thiadiazol-4-yl)thiophen-2-yl)phosphonate (2.1)

To an oven dried (OD) 500 mL Schlenk flask, equipped with a stir bar, 4,7-dibromobenzo[*c*][1,2,5]thiadiazole (12.9 g, 43.9 mmol, 2 equivalents (equiv.)), diethyl (5-(trimethylstannyl)thiophen-2-yl)phosphonate (8.4 g, 21.9 mmol, 1 equiv.), tris(dibenzylideneacetone)dipalladium (0.40 g, 0.44 mmol, 0.02 equiv.), and Tri(*o*-tolyl)phosphine (0.60 g, 1.97 mmol, 0.09 equiv.) were added. A rubber septum was affixed and the flask was evacuated for 5 minutes (min). $Ar_{(g)}$ was introduced and then toluene from the solvent purification system (SPS) (269 mL, 232.6 g, 2524 mmol, 115 equiv.) was added via cannula (15 gauge). The mixture was degassed using the freeze-pump-thaw (FPT) technique four times. The mixture was brought to 90 °C and stirred for 13 hours in an $Ar_{(g)}$ atmosphere. The solvent was removed under reduced pressure. The crude material was run through a pad of neutral silica (d=8.5 cm, h=3 cm) using 10% methanol (MeOH) in dichloromethane (DCM) in order to remove palladium and unreacted dibromobenzo[*c*][1,2,5]thiadiazole. The mixture (~9 g) was then chromatographed twice using neutral silica (1st column: d=6.5 cm, h=29 cm, 2nd column: d=4 cm, h=29 cm) and 97:3 DCM:MeOH to yield an oily orange solid (9.50 g, 41%). ^{1}H NMR (300 MHz, $CDCl_3$): δ (ppm) 8.09 (t, 1H), 7.90 (d, 1H), 7.79 (d, 1H), 7.72 (q, 1H), 4.20 (m, 4H), 1.38 (t, 6H). HR-MALDI-MS: m/z = 432.9442^{+}, $[M+H]^{+}$ = 432.9445.

Diethyl (5-(7-(thiophen-2-yl)benzo[*c*][1,2,5]thiadiazol-4-yl)thiophen-2-yl)phosphonate (2.2)

To an OD 200 mL Schlenk flask, equipped with a stir bar, diethyl (5-(7-bromobenzo[*c*][1,2,5]thiadiazol-4-yl)thiophen-2-yl)phosphonate (3.86 g, 8.91 mmol, 1 equiv.), 2-(tributylstannyl)thiophene (3.50 mL, 4.11 g, 11.02 mmol, 1.2 equiv.), tris(dibenzylideneacetone)dipalladium (0.17 g, 0.18 mmol, 0.02 equiv.), and Tri(*o*-tolyl)phosphine (0.25 g, 0.82 mmol, 0.09 equiv.) were added. A rubber septum was affixed and the flask was evacuated for 3 min. $Ar_{(g)}$ was introduced and then SPS toluene (105 mL, 90.8 g, 986 mmol, 115 equiv.) was added via cannula (15 gauge). The mixture was degassed using FPT three times. The mixture was brought to 90 °C and stirred for 14 hours in an $Ar_{(g)}$ atmosphere. The solvent was removed under reduced pressure. The crude material was run through a pad of neutral silica (d=8 cm, h=3 cm) using a gradient from 0% to 10% MeOH in DCM in order to remove palladium and unreacted starting materials. The mixture was then chromatographed using neutral silica (d=7.5 cm, h=30 cm) and 97:3 DCM:MeOH to yield an orange oil (3.61 g, 93%). ^{1}H NMR (300 MHz, $CDCl_3$): δ (ppm) 8.16 (dd, 1H), 8.12 (dd, 1H), 7.95 (d, 1H), 7.90 (d, 1H), 7.73 (q, 1H), 7.49 (dd, 1H), 7.23 (dd, 1H), 4.20 (m, 4H), 1.38 (t, 6H). HR-MALDI-MS: *m/z* = 437.0238$^+$, $[M+H]^+$ = 437.0217.

Diethyl (5-(7-(5-bromothiophen-2-yl)benzo[*c*][1,2,5]thiadiazol-4-yl)thiophen-2-yl)phosphonate (2.3)

To a flame dried 200 mL Schlenk flask, equipped with a stir bar, diethyl (5-(7-(thiophen-2-yl)benzo[*c*][1,2,5]thiadiazol-4-yl)thiophen-2-yl)phosphonate (2.88 g, 6.59 mmol, 1 equiv.) was added. A rubber septum was affixed and the flask was evacuated for 5 min.

$Ar_{(g)}$ was introduced and then SPS tetrahydrofuran (THF) (80 mL, 71.1 g, 986 mmol, 150 equiv.) was added via cannula (15 gauge). The mixture was stirred to dissolve the starting material and cooled to 0 °C. NBS (1.23 g, 6.92 mmol, 1.05 equiv.) was added over an inert atmosphere. The mixture was stirred for 10 min in the dark at 0 °C, warmed to room temperature (r.t.) while stirring for 4 hours, and finally refluxed for 19 hours in the dark while stirring. Extracted the product into DCM and washed three times with deionized (DI) H_2O. Dried the organic phase with $MgSO_4$ and filtered it through a coarse glass frit. Removed the solvent under reduced pressure. The mixture was then chromatographed using neutral silica (d=7.5 cm, h=16 cm) and 97:3 DCM:MeOH to yield an orange/red solid (3.26 g, 96%). ^{1}H NMR (300 MHz, $CDCl_3$): δ (ppm) 8.12 (t, 1H), 7.94 (d, 1H), 7.84 (d, 1H), 7.83 (d, 1H), 7.73 (q, 1H), 7.17 (d, 1H), 4.21 (m, 4H), 1.38 (t, 6H). HR-MALDI-MS: m/z = 514.9335$^+$, $[M+H]^+$ = 514.9322.

Diethyl (5-(7-(5-(4-([2,2':6',2''-terpyridin]-4'-yl)phenyl)thiophen-2-yl)benzo[*c*][1,2,5]thiadiazol-4-yl)thiophen-2-yl)phosphonate (2.4)

To a flame dried 100 mL Schlenk flask, equipped with a stir bar, diethyl (5-(7-(5-bromothiophen-2-yl)benzo[*c*][1,2,5]thiadiazol-4-yl)thiophen-2-yl)phosphonate (1.23 g, 2.34 mmol, 1 equiv.) and 4'-(4-(tributylstannyl)phenyl)-2,2':6',2''-terpyridine (1.46 g, 2.44 mmol, 1.02 equiv.) were added. A rubber septum was affixed and the flask was evacuated for 5 min. $Ar_{(g)}$ was introduced and then SPS toluene (29.5 mL, 25.5 g, 277 mmol, 116 equiv.) was added via syringe (18 gauge). The mixture was degassed using FPT two times. Tetrakis(triphenylphosphine)palladium(0) (0.44 g, 0.38 mmol, 0.16 equiv.) was added over an inert atmosphere. The mixture was degassed using FPT three times. The mixture was brought to 110 °C and stirred for 66 hours in an $Ar_{(g)}$ atmosphere. The

solvent was removed under reduced pressure. The crude material was run through a pad of neutral alumina (d=9 cm, h=3 cm) using a gradient from 0% to 5% MeOH in DCM in order to remove palladium and unreacted starting materials. The mixture (~3.5 g) was then chromatographed using neutral alumina (d=9 cm, h=30 cm) and 97:3 DCM:MeOH. The product was then precipitated into hexanes 3 times to yield a wine red solid (1.24 g, 70%). ^{1}H NMR (300 MHz, $CDCl_3$): δ (ppm) 8.78 (s, 2H), 8.75 (d, 2H), 8.68 (d, 2H), 8.18 (d, 1H), 8.13 (t, 1H), 7.91 (m, 8H), 7.74 (q, 1H), 7.53 (d, 1H), 7.37 (ddd, 1H), 4.22 (m, 4H), 1.39 (t, 6H). HR-MALDI-MS: m/z = 744.1364$^+$, $[M+H]^+$ = 744.1327.

[Ru(tpy)(bpy)Cl-T-BTD-T-PO_3Et_2]PF_6 (2.5)

To a 30 mL microwave vial, equipped with a stir bar, diethyl (5-(7-(5-(4-([2,2':6',2''-terpyridin]-4'-yl)phenyl)thiophen-2-yl)benzo[*c*][1,2,5]thiadiazol-4-yl)thiophen-2-yl)phosphonate (0.30 g, 0.40 mmol, 1 equiv.) and [Ru(bpy)(η^6-Bz)(Cl)]Cl (0.16 g, 0.40 mmol, 1 equiv.) were added. The headspace was purged with $Ar_{(g)}$ for 5 min. Ethanol (8.44 mL, 6.6 g, 144.5 mmol, 358 equiv.) and DI H_2O (4.23 mL, 4.23 g, 234.7 mmol, 582 equiv.) were combined in a ~2:1 ratio and degassed by bubbling $Ar_{(g)}$ into the solvent mixture for 5 min. The solvent system was added to the microwave vial and the mixture was heated in the microwave on dynamic mode for 20 min at 160 °C (300 W, 300 psi). The solvent was removed under reduced pressure. The crude material was suspended in MeOH then filtered and washed with MeOH until the drip was colorless. The solvent was removed under reduced pressure. The product was suspended in a 6:1 v:v H_2O:MeOH solution and a large excess of NH_4PF_6 as a solution in H_2O was added. The mixture was stirred for 2 hours and a wine red colored precipitate crashed out. The precipitate was filtered and washed with H_2O. The residue was then washed into a flask using ACN and

the solvent was removed under reduced pressure. The crude product was purified via PTLC on neutral alumina (1000 μm thickness, 20 cm x 20 cm) using 30% ACN in DCM to yield a wine red solid (0.08 g,17%). ^{1}H NMR (300 MHz, CD_3CN): δ (ppm) 10.28 (d, 1H), 8.79 (s, 2H), 8.61 (d, 1H), 8.55 (d, 2H), 8.30 (t, 2H), 8.26-7.95 (m, 10H), 7.90 (dt, 2H), 7.75-7.65 (m, 5H), 7.39 (d, 1H), 7.29 (t, 2H), 6.97 (t, 1H), 4.24-4.10 (m, 4H), 1.35 (t, 6H). HR-MALDI-MS: m/z = 1036.0668$^+$, $[M]^+$ = 1036.0668.

$[Ru(tpy)(bpy)CH_3CN\text{-}T\text{-}BTD\text{-}T\text{-}PO_3H_2]^{2+}$ (2.6)

To a 25 mL Schlenk tube, equipped with a stir bar, $[Ru(tpy)(bpy)Cl\text{-}T\text{-}BTD\text{-}T\text{-}PO_3Et_2]PF_6$ **(2.5)** (0.010 g, 0.008 mmol, 1 equiv.) was added. A rubber septum was affixed and the flask was evacuated for 15 min. $Ar_{(g)}$ was introduced and then DCM (2 mL, 2.66 g, 31.3 mmol, 3701 equiv.) was added via syringe (21 gauge). The Schlenk tube was sonicated to suspend the starting material. Trimethylsilyl bromide (0.5 mL, 0.58 g, 3.79 mmol, 448 equiv.) was added via syringe (21 gauge) and the reaction was stirred for 5 hours. The solvent, remaining trimethylsilyl bromide**,** and the suspected byproduct (ethyl bromide) were removed under reduced pressure. A rubber septum was affixed and the flask was evacuated for 15 min. $Ar_{(g)}$ was introduced and then MeOH (5 mL, 3.95 g, 123.4 mmol, 14585 equiv.) was added via syringe (21 gauge). The Schlenk tube was sonicated to suspend the starting material and the mixture was stirred at r.t. for 30 min. The solvent and the suspected byproduct (methoxytrimethylsilane) were removed under reduced pressure to afford a wine red solid. The solid was dried under vacuum overnight. $Ar_{(g)}$ was introduced and then DCM (5 mL, 6.65 g, 78.3 mmol, 9251 equiv.) was added via syringe (21 gauge). The Schlenk tube was sonicated to suspend the wine red solid. The suspension was cooled to 0 °C while stirring. Triflic acid (0.5 mL, 0.85 g, 5.66

mmol, 669 equiv.) was added dropwise over 15 s under an inert atmosphere. The suspension immediately turned dark green. The rubber septum was affixed and the suspension was stirred for 10 min while allowing the tube to warm to r.t.. The suspension was precipitated into 150 mL of 0 °C ether. The solid immediately turned red again. The cold suspension in ether was filtered through a stack of two Teflon filters and washed with ether to afford an orange/red solid (0.0058 g, 53%). ^{1}H NMR (300 MHz, CD_3CN): δ (ppm) 9.63 (d, 1H), 8.96-8.81 (m, 2H), 8.63 (t, 3H), 8.42-7.20 (m, 21H), 7.11 (t, 1H). HR-ESI-MS (ACN): $m/z = 493.0291^{2+} = 986.0582$, $[M]^{2+} = 986.06$.

2.3.2 ^{1}H Nuclear Magnetic Resonance

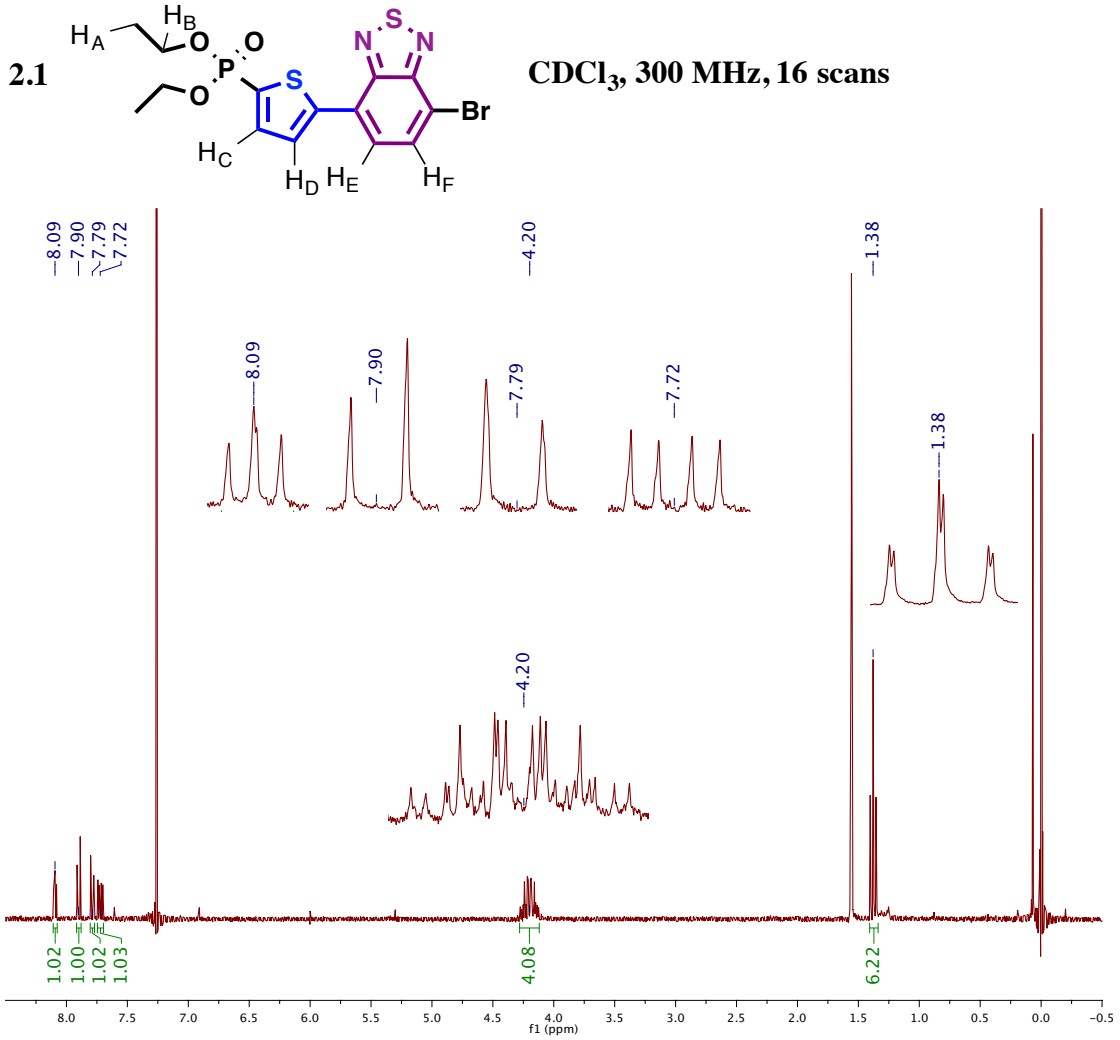

Figure 2.2: ^{1}H NMR spectrum of compound **2.1**.

Referring to Figure 2.2, protons H_A and H_B are present in the ^{1}H NMR spectra of compounds **2.1** – **2.5**. They take the form of a 6H triplet at ~1.3 ppm and a 4H multiplet at ~4.2 ppm respectively. Proton H_B would show up as a quartet if strong coupling with the P nuclei were not present. Protons H_C and H_D remain practically stationary during the progression from compound **2.1** to **2.6** and maintain the 1H triplet (~8.1 ppm) and 1H quartet (~7.7 ppm) splitting patterns as a result of being far away from the sites of

structural modification. Protons H_E and H_F at ~7.9 and ~7.8 ppm belong to the accepting unit drawn in purple. The two 1H doublets are easily identified in the development from compound **2.1** to **2.3**, but afterwards become difficult to pick out due to an increasing number of aromatic signals that begin overlapping with one another.

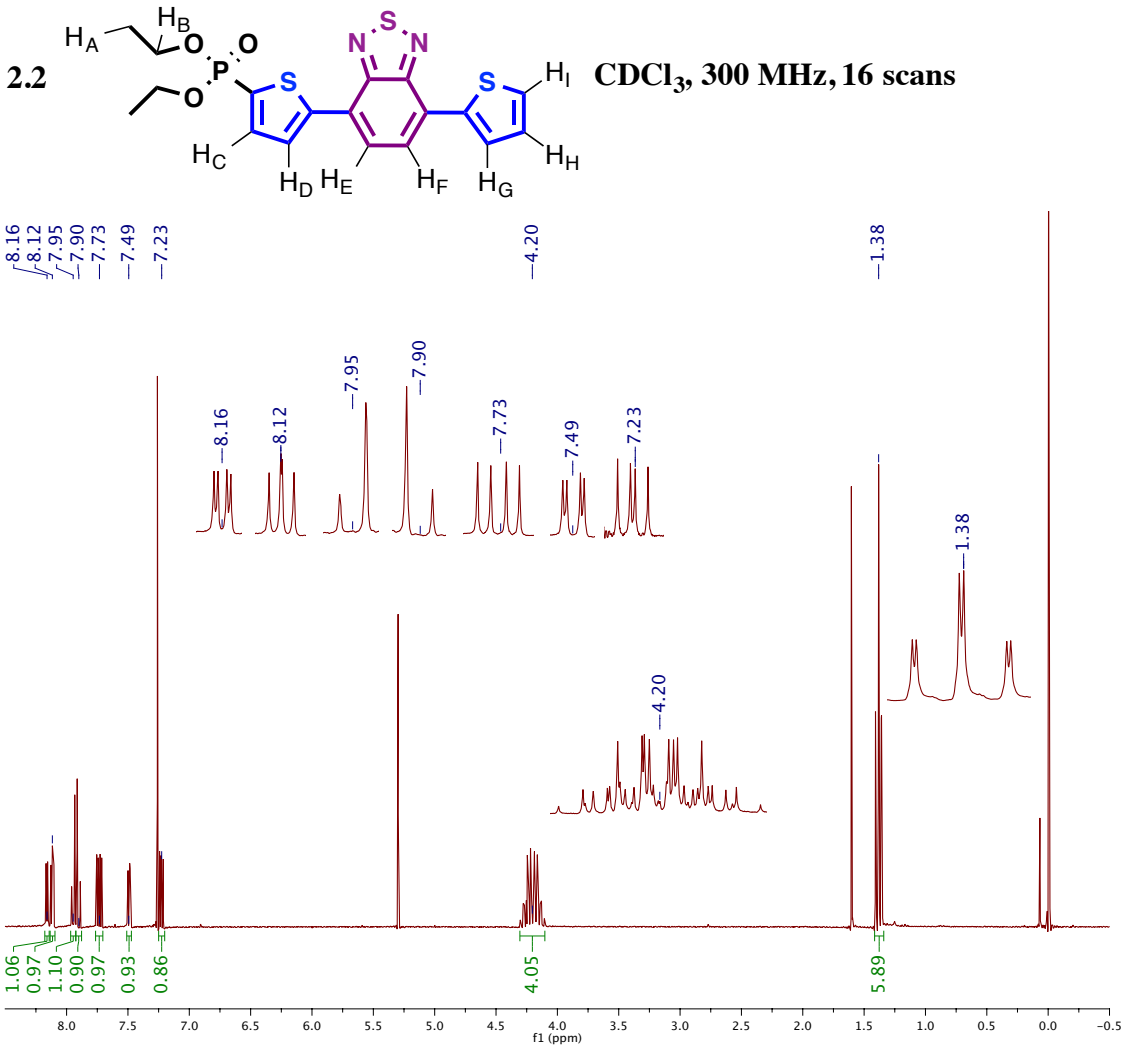

Figure 2.3: ^{1}H NMR spectrum of compound **2.2**.

Figure 2.3 is evidence of three new aromatic protons present in the product: three 1H doublets of doublets at 8.16 ppm, 7.49 ppm, and 7.23 ppm. H_G is closest to the deshielding ring currents of the acceptor moiety in purple, making it likely that it is the furthest downfield signal at 8.16 ppm.

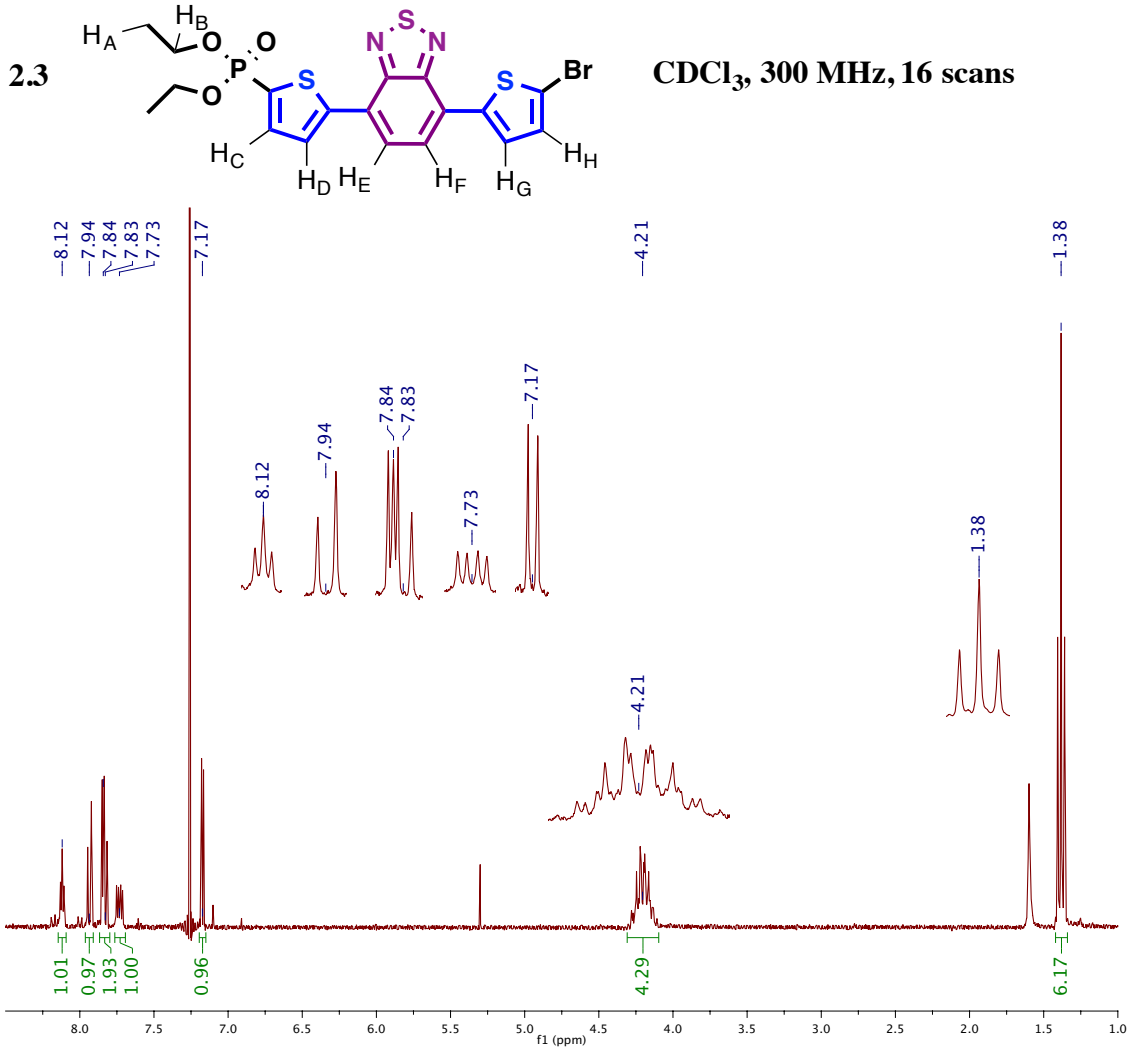

Figure 2.4: ^{1}H NMR spectrum of compound **2.3**.

Figure 2.4 depicts a change in the coupling between protons H_G and H_H, now at ~7.83 and 7.17 ppm respectively. Doublets are observed which makes sense with the replacement of the former coupling partner H_I for bromine. The large, polarizable bromine also has an appreciable effect on the chemical shift of H_G, moving it upfield by 4%. Bromine is able to donate its π-electrons into the thiophene ring and add electron density to the meta positions like H_G.

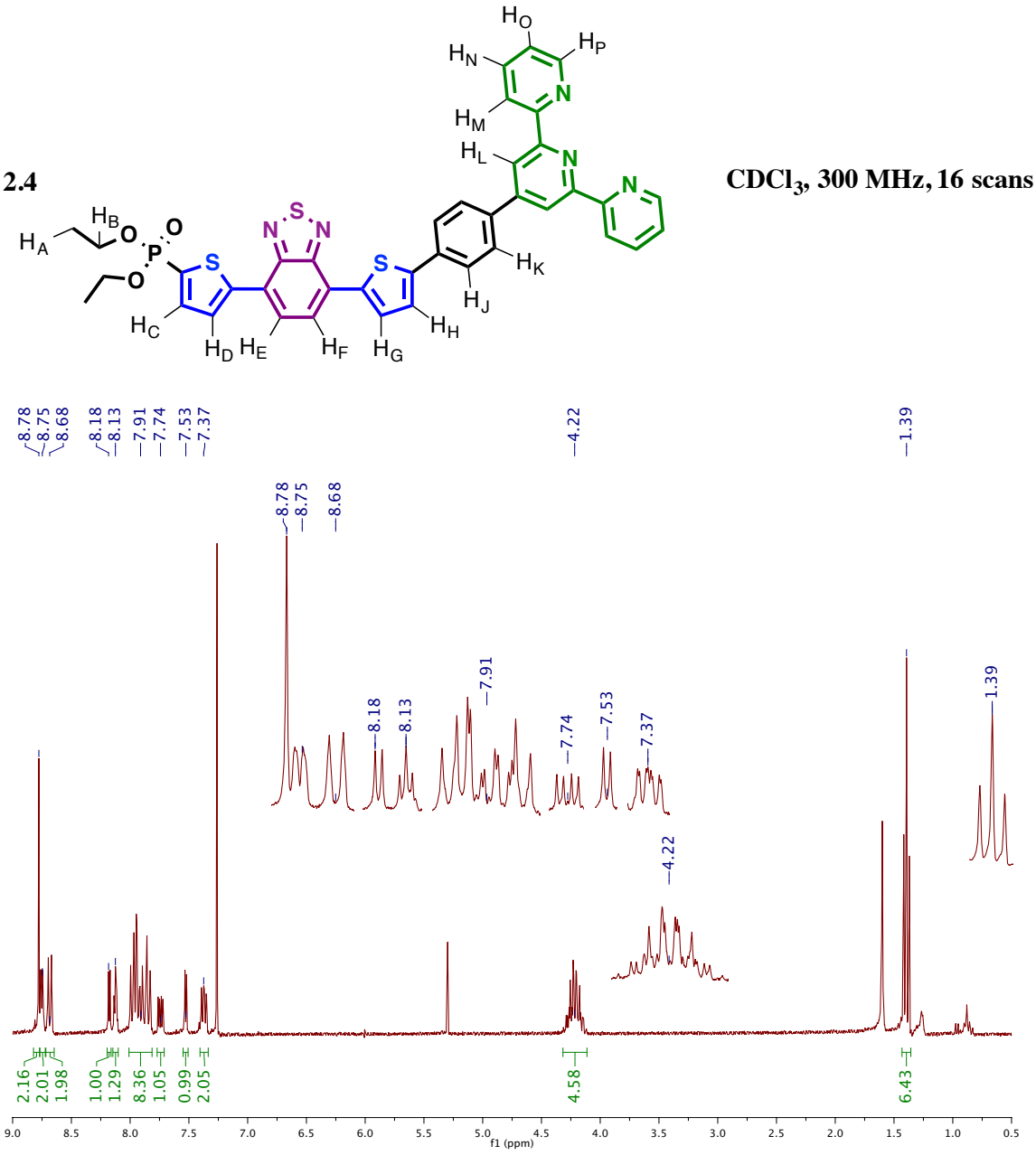

Figure 2.5: ^{1}H NMR spectrum of compound **2.4**.

Adding the terpyridine ligand in green, linked through the benzene ring in black, makes the identification of many of the peaks very difficult in Figure 2.5. Thirteen ideally unique aromatic protons, comprising 20 aromatic protons in total, now belong to the system. The key signal to look for as evidence of desired product formation is a 2H singlet belonging to H_L that would theoretically be as downfield or more than other

protons in the system that are surrounded by ring currents on each side (H_F previously at ~7.94 or 7.84 ppm and H_G previously at ~7.83 ppm). Indeed there is a 2H singlet at 8.78 ppm, which belongs to H_L. In addition The signature 1H triplet (8.13 ppm) and quartet (7.74 ppm) of protons H_C and H_D remain easily observable.

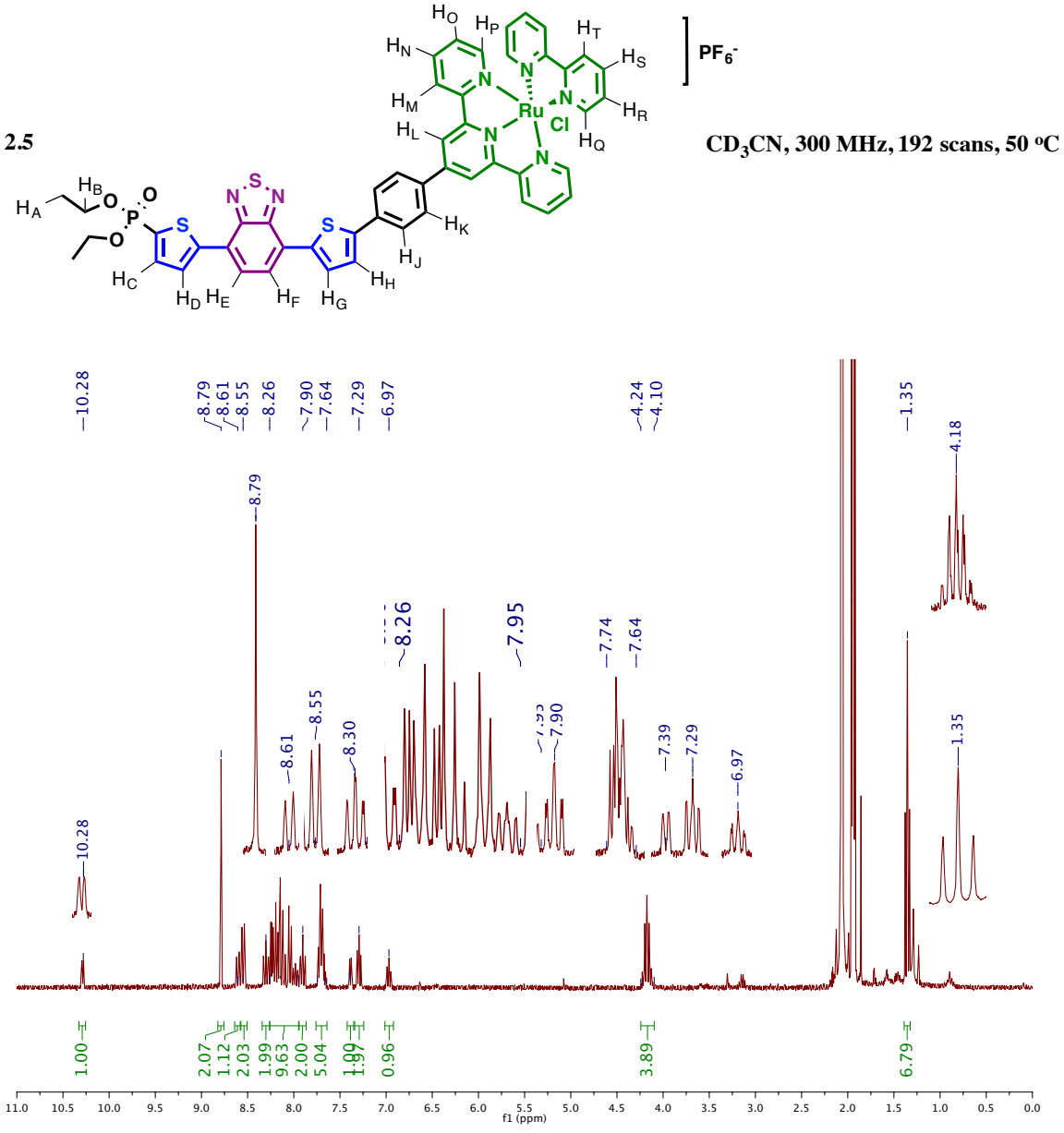

Figure 2.6: ^{1}H NMR spectrum of compound **2.5**.

The task of identifying each individual signal without employing 2D NMR techniques becomes nearly impossible with the final coordination of the bipyridine ligand to make compound **2.5**. Figure 2.6 depicts a convoluted ^{1}H NMR spectrum, but fortunately the research group of Curtis P. Berlinguette acquired ^{1}H NMR data on similar Ru(tpy)(bpy) chloro-ligated systems in acetonitrile and observed a 1H doublet at 10.20 ppm corresponding to H_Q, the proton on the bpy ring nearest the chloro- ligand.[18] Likewise, a 1H doublet at 10.28 ppm is observed for compound **2.5**; as well as, the 2H singlet of H_L at 8.79 ppm.

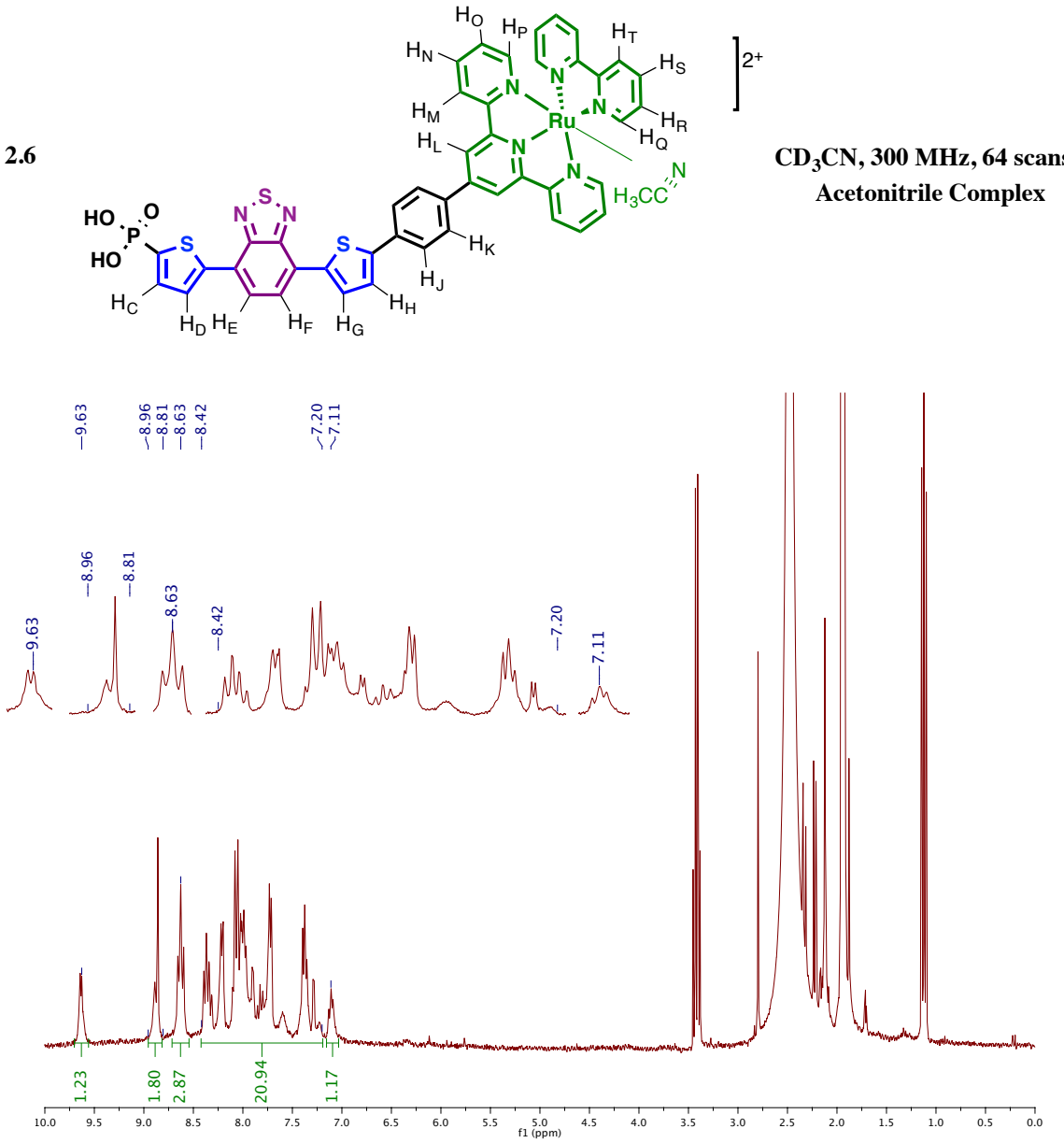

Figure 2.7: ^{1}H NMR spectrum of compound **2.6**.

As evidenced in Figure 2.7, in the final two steps of deprotecting the acid and the active site of the ruthenium, the 6H H_A (~1.3 ppm) and 4H H_B (~4.2 ppm) signals are finally lost and the signal H_Q moves downfield by 6% to 9.63 ppm. The exchange of the electronegative, polarizable chlorine for the acetonitrile ligand returned electron density to H_Q causing it to shift upfield.

2.3.3 Mass Spectrometry

2.1 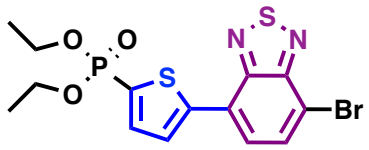

***m/z:* 432.94 [M+H]⁺**

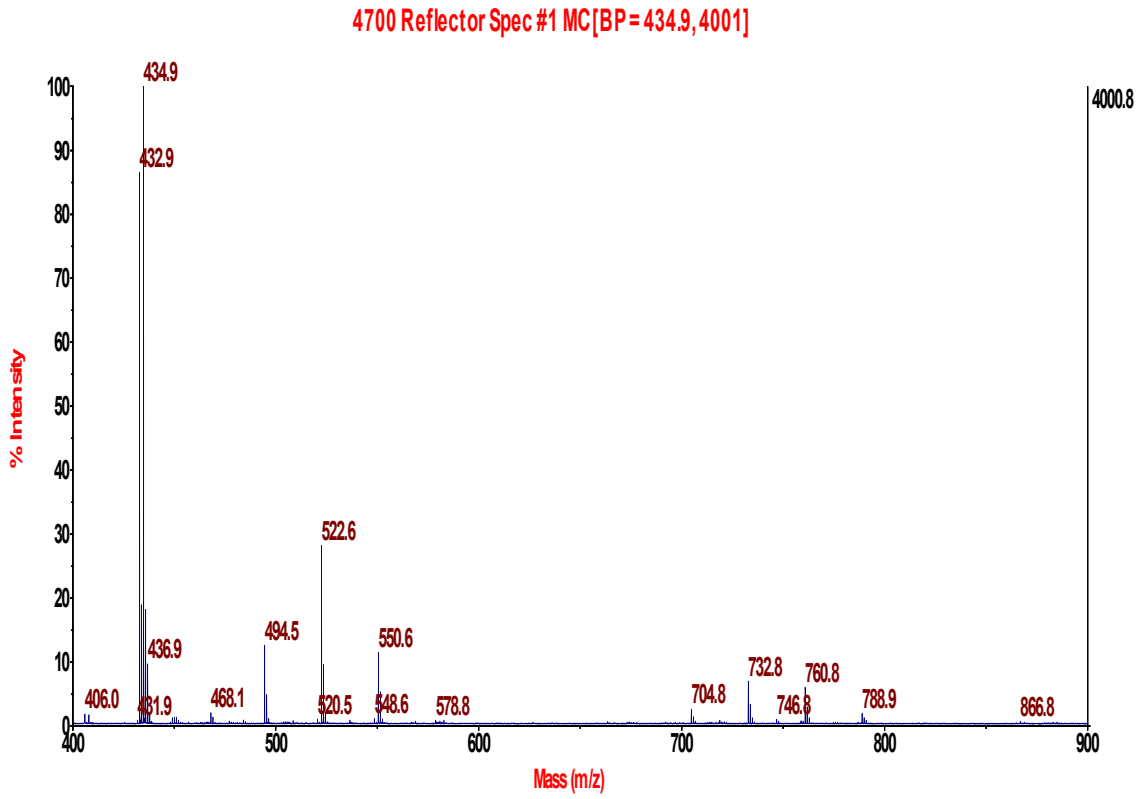

Figure 2.8: Matrix-assisted laser desorption/ionization – time of flight (MALDI-TOF) spectrum of compound **2.1**.

In addition to ^{1}H NMR, low and high-resolution mass spectra were acquired for compounds **2.1** – **2.6** to further confirm the identity of the product. Figure 2.8 depicts a characteristic MALDI $[M+H]^+$ signal of 432.9, which matches the predicted mass-to-charge ratio (m/z) $[M+H]^+$ value of 432.94 based on monoisotopic masses.

2.2

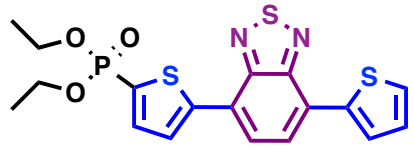

***m/z:* 437.01 [M+H]⁺**

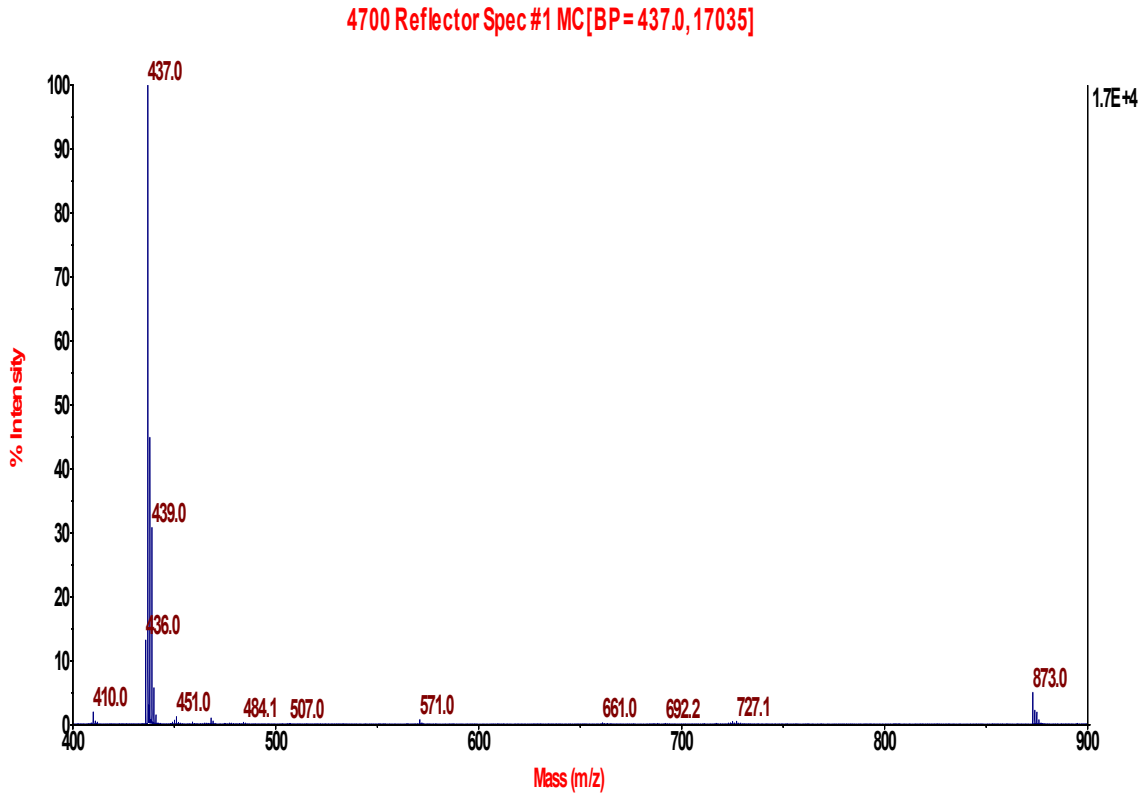

Figure 2.9: MALDI-TOF spectrum of compound **2.2**.

Figure 2.9 depicts a characteristic MALDI $[M+H]^+$ signal of 437.0, which matches the predicted m/z $[M+H]^+$ value of 437.01 based on monoisotopic masses.

2.3 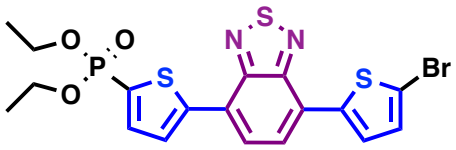

***m/z:* 514.92 [M+H]$^+$**

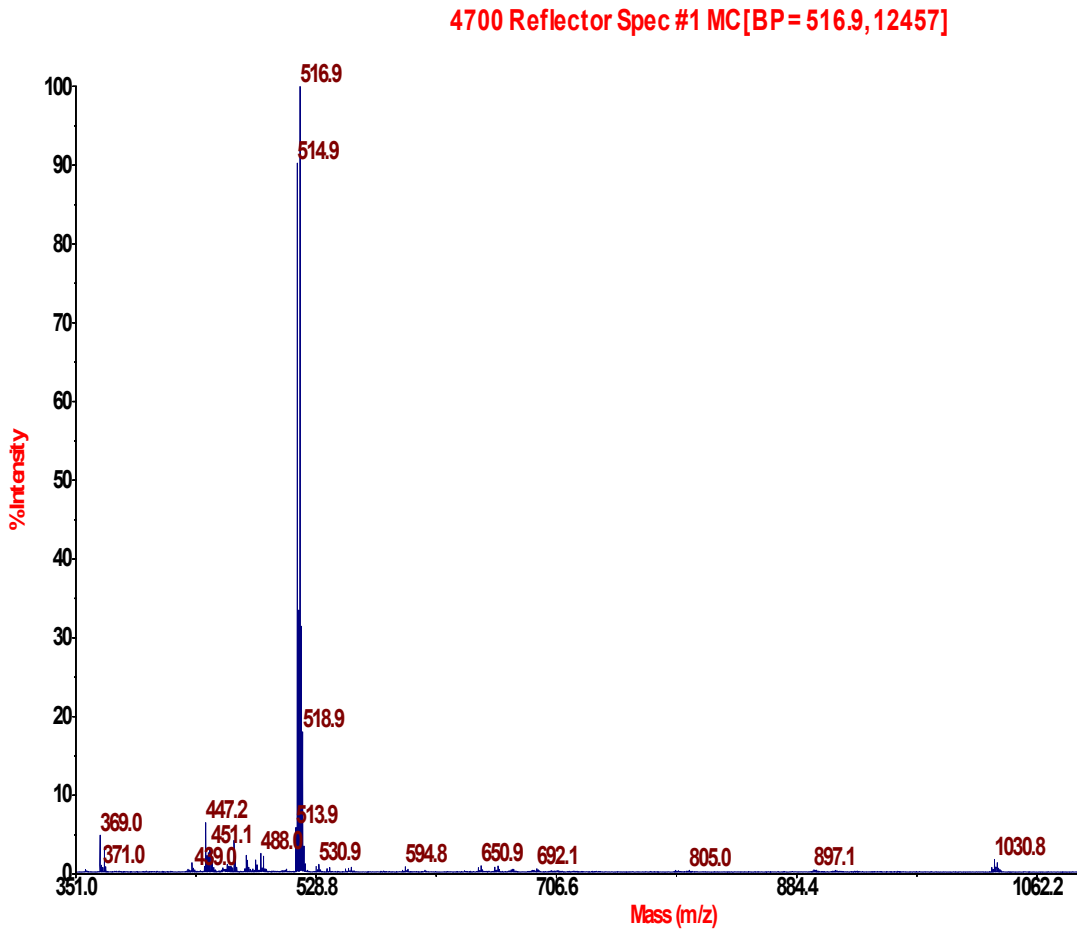

Figure 2.10: MALDI-TOF spectrum of compound **2.3**.

Figure 2.10 depicts a characteristic MALDI [M+H]$^+$ signal of 514.9, which matches the predicted m/z [M+H]$^+$ value of 514.92 based on monoisotopic masses.

2.4

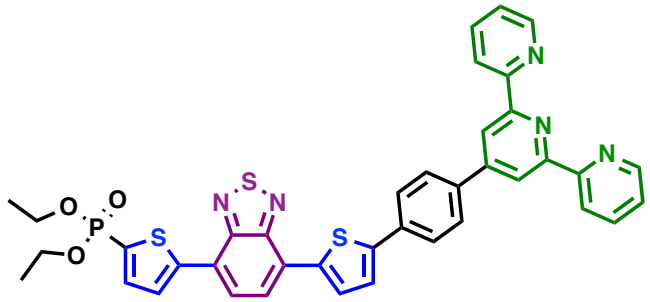

***m/z:* 744.12 [M+H]$^+$**

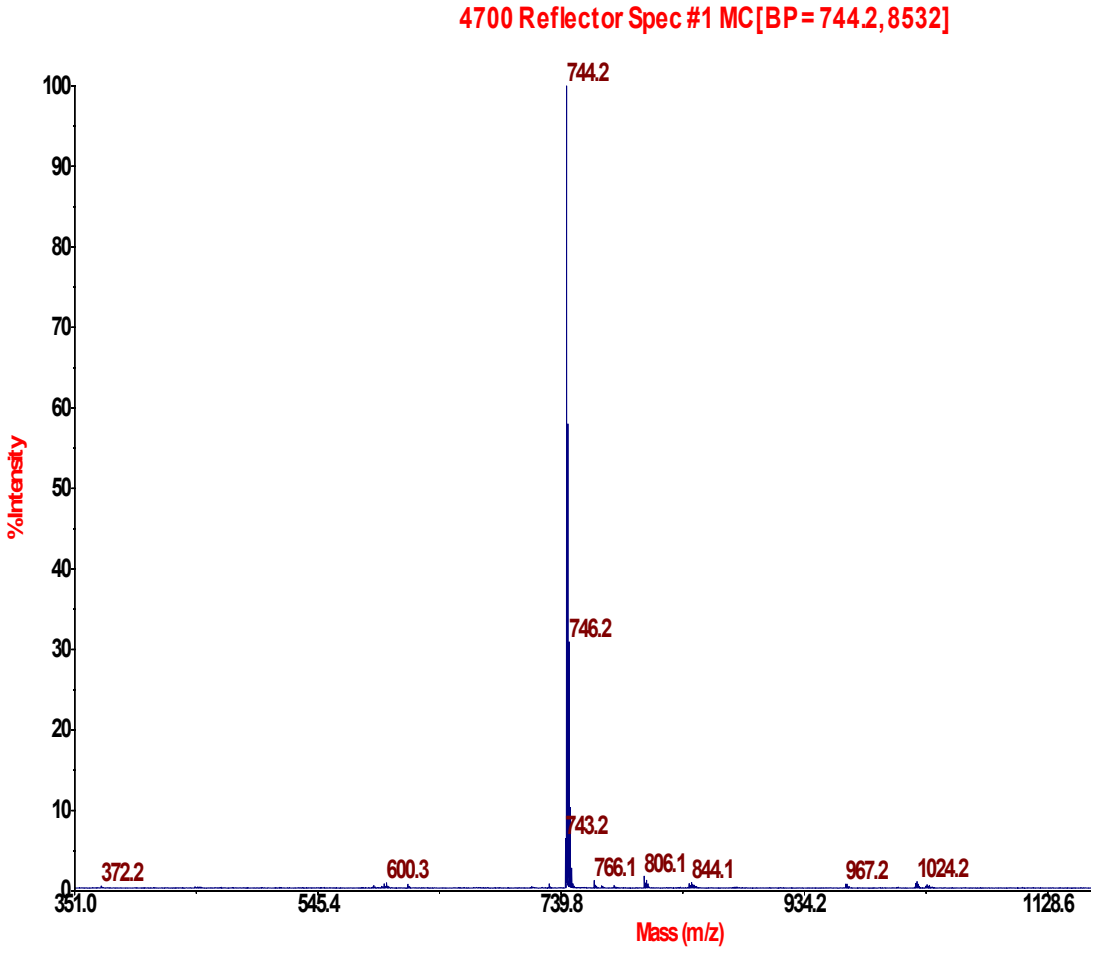

Figure 2.11: MADLI-TOF spectrum of compound **2.4**.

Figure 2.11 depicts a characteristic MALDI $[M+H]^+$ signal of 744.2, which matches the predicted m/z $[M+H]^+$ value of 744.12 based on monoisotopic masses.

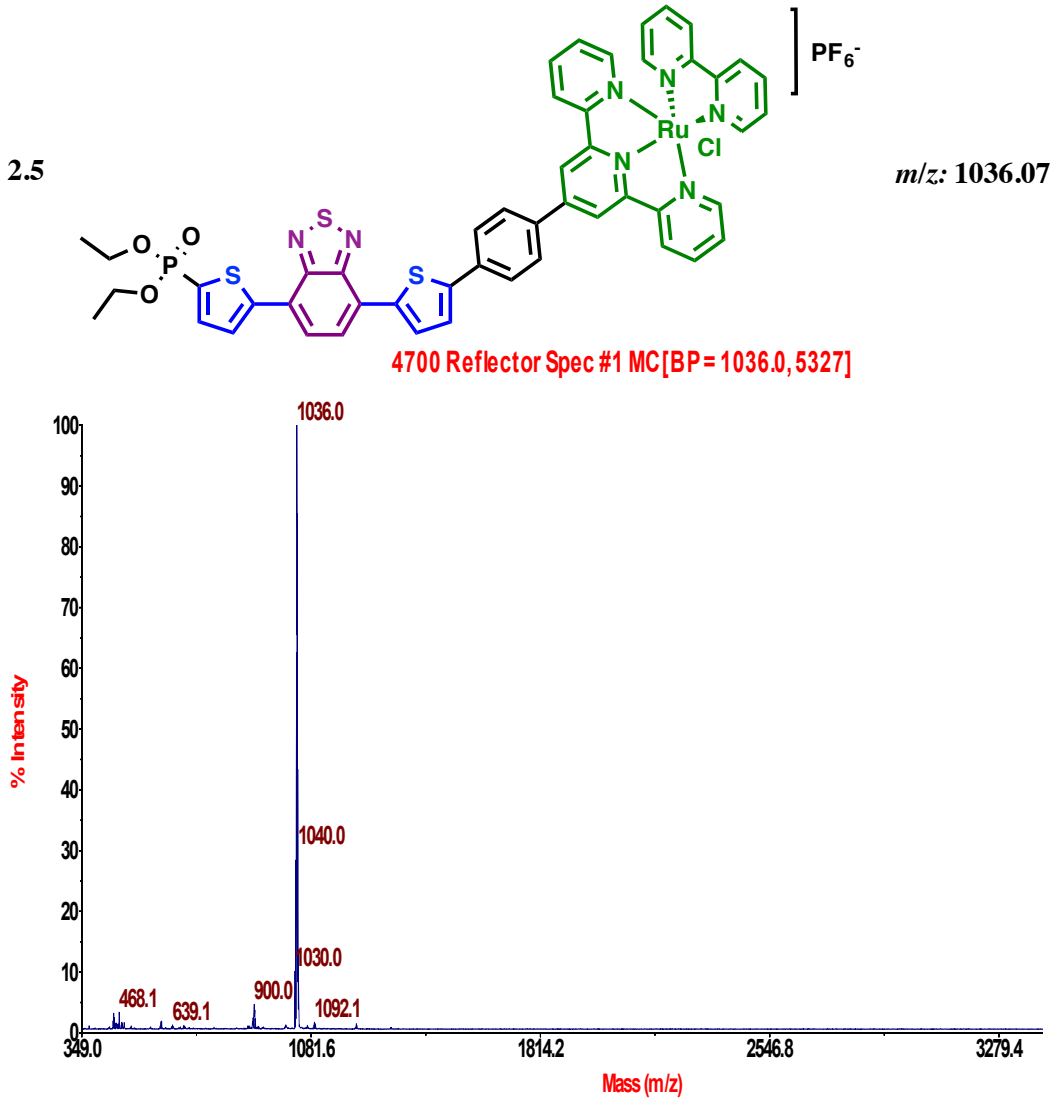

Figure 2.12: MADLI-TOF spectrum of compound **2.5**.

Figure 2.12 depicts a less common MALDI molecular ion ($[M]^+$) signal of 1036.0, which matches the predicted m/z $[M]^+$ value of 1036.07 based on monoisotopic masses.

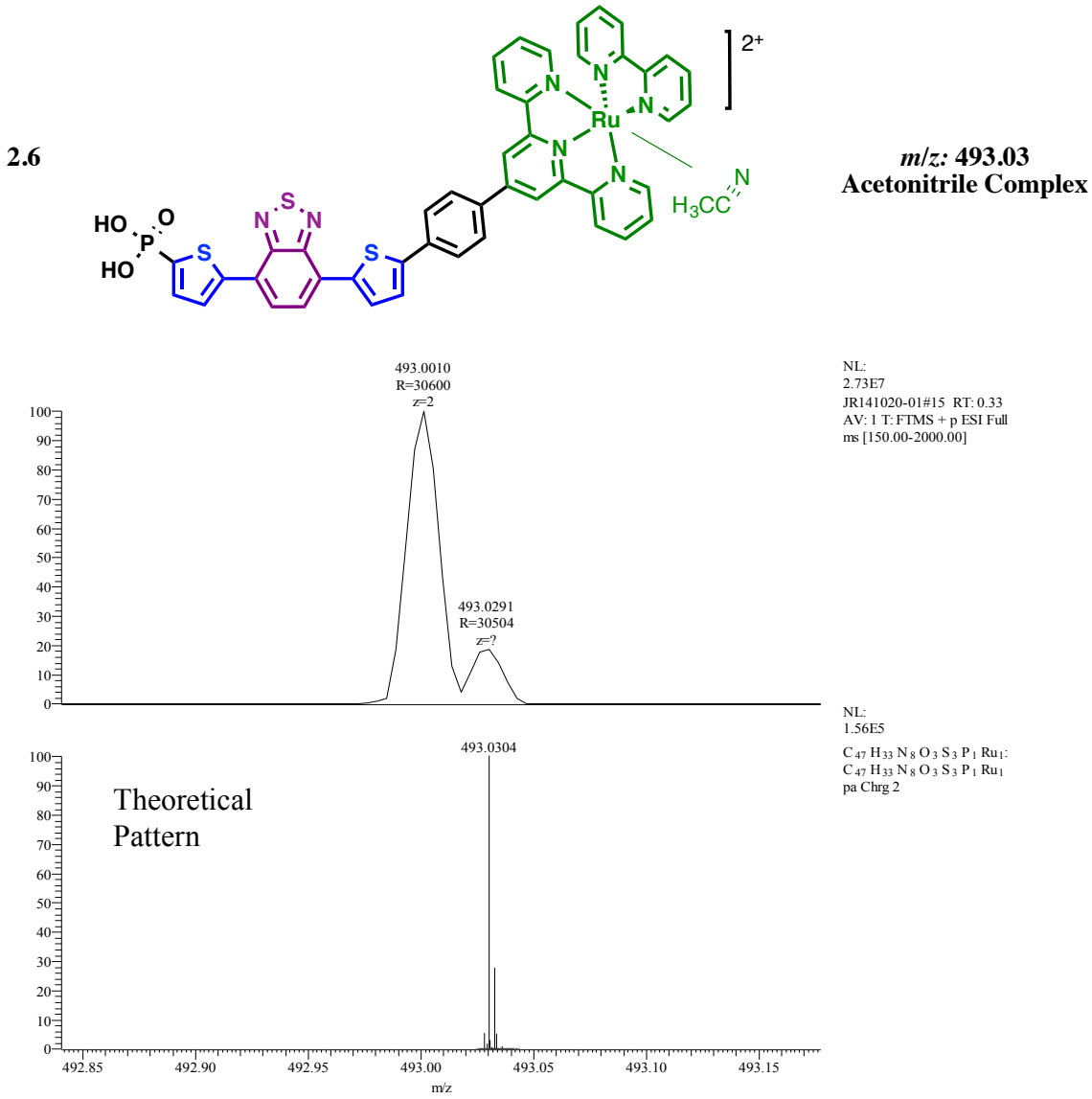

Figure 2.13: ESI spectrum of compound **2.6**.

Figure 2.13 depicts a characteristic electrospray ionization (ESI) $[M]^{2+}$ signal of 493.0010, which matches the predicted m/z $[M]^{+}$ value of 493.03 based on monoisotopic masses.

2.4 ULTRAVIOLET-VISABLE SPECTROSCOPY

Solution UV-Vis experiments in acetonitrile were conducted on chromophore **2.4**, chromophore-catalyst assembly **2.5**, and a model catalyst to compare light absorbing capabilities and spectral coverage. Figure 2.14 indicates enhanced optical absorption of T-BTD-T-catalyst assembly **2.5** relative to the model catalyst. The broad absorption of the assembly suggests electronic communication between the T-BTD-T chromophore and the Ru(tpy)(bpy) catalyst.

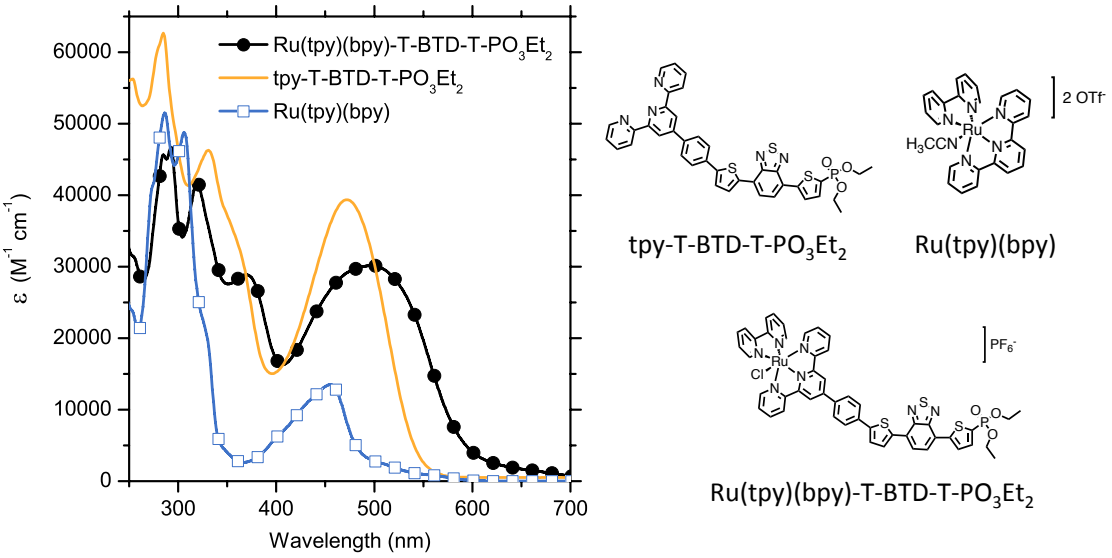

Figure 2.14: Improved light capture and broadening of spectral range of chromophore-catalyst assembly 2.5 (black) relative to model catalyst (blue) and chromophore 2.4 (orange) respectively.

The UV-Vis spectrum of Ru(tpy)(bpy)-T-BTD-T-PO_3Et_2 **2.5** compared with the UV-Vis spectrum of Ru(tpy)(bpy)-T_3-PO_3H_2 **1.5** evidenced in Figure 2.15 is red-shifted. The water oxidation experiment for **2.5** needs to be conducted as it was for **1.5** in Figure 1.11 and the results need to be compared to determine whether or not **2.5** acts as a better water oxidation chromophore-catalyst assembly than **1.5**. Romain Stalder's data in Figure 1.8

that shows the 2-fold increase in photocurrent and device efficiency (DSSCs) for the donor-acceptor **T4BTD-A** relative to the all donor **T6-A** suggests that the donor-acceptor chromophore-catalyst assembly **2.5** will perform water oxidation better than **1.5**.

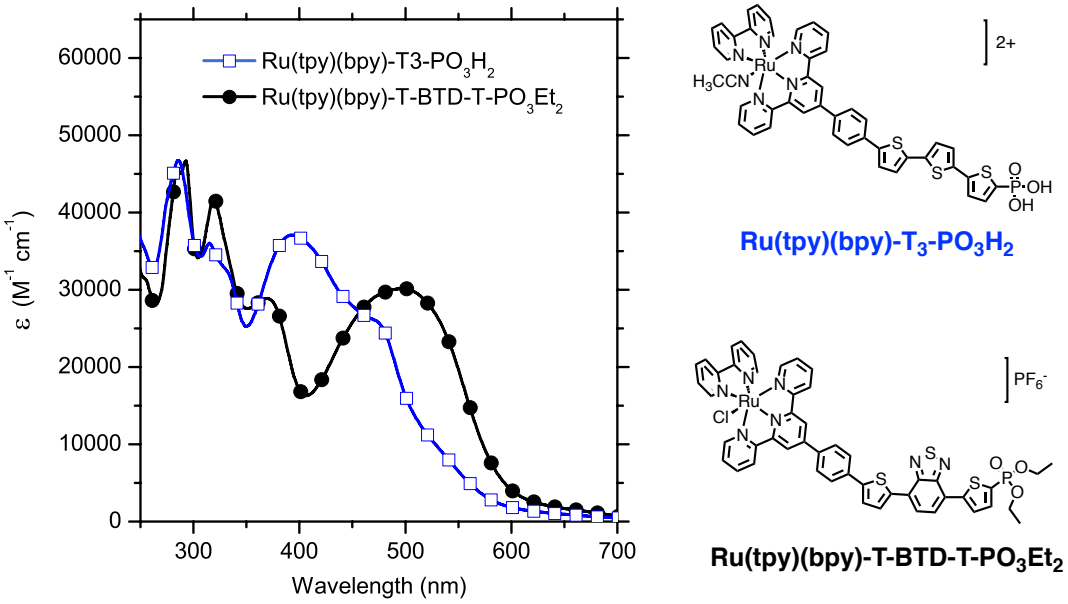

Figure 2.15: Comparison of T_3 **1.5** (blue) with T-BTD-T **2.5** (black) assemblies in acetonitrile (ACN).

CHAPTER 3

CONCLUSION AND OUTLOOK

This thesis presented the successful synthesis of a novel chromophore-catalyst assembly designed to leverage the light harvesting ability of the chromophore to drive an electron transfer process that splits water into oxygen and protons at the catalyst. The novelty of the work lies in utilizing an organic chromophore of a donor-acceptor type nature to harvest the light as opposed to using an organic chromophore of an all donor type nature or an inorganic chromophore like the ones used by Thomas J. Meyer in 2012 that are ruthenium based.[5] Donor-acceptor interactions lower the bandgaps of molecules relative to structurally similar all donor moieties, decreasing the amount of energy needed to excite an electron. If comparable photocurrents can be generated using less energetic light, and oxygen evolution experiments can produce similar results, then the process will be made more efficient overall by utilizing donor-acceptor moieties.

Evidence of a lower bandgap is seen in the red-shifted absorbance maximum of the donor-acceptor chromophore-catalyst assembly relative to the all donor terthiophene system synthesized by Toan V. Pho. The ability of the donor-acceptor chromophore-catalyst assembly to transform light into current compared with the all donor assembly remains to be discovered. For future work, the photocurrent experiment of the donor-acceptor assembly needs to be done and the oxygen evolution experiments of the all donor and donor-acceptor assemblies need to be conducted. Also, if those experiments provide promising results, lifecycle testing will be needed to determine the TN of the assembly.

REFERENCES

(1) Stalder, R.; Xie, D.; Islam, A.; Han, L.; Reynolds, J. R.; Schanze, K. S. *ACS Appl. Mater. Interfaces* **2014**, *6*, 8715.

(2) Kärkäs, M. D.; Verho, O.; Johnston, E. V; Akermark, B. *Chem. Rev.* **2014**.

(3) Song, W.; Chen, Z.; Brennaman, M. K.; Concepcion, J. J.; Patrocinio, A. O. T.; Murakami Iha, N. Y.; Meyer, T. J. *Pure Appl. Chem.* **2011**, *83*, 749.

(4) Why Life: Tackling the Global Energy Crisis. https://life.llnl.gov/why_life/index.php/ (accessed December 15, 2014).

(5) Ashford, D. L.; Song, W.; Concepcion, J. J.; Glasson, C. R. K.; Brennaman, M. K.; Norris, M. R.; Fang, Z.; Templeton, J. L.; Meyer, T. J. *J. Am. Chem. Soc.* **2012**, *134*, 19189.

(6) Kudo, A.; Miseki, Y. *Chem. Soc. Rev.* **2009**, *38*, 253.

(7) Honda, K.; Fujishima, A. *Nature* **1972**, *238*, 37.

(8) Kazuhito; Irie, H.; Fujishima, A. *Jpn. J. Appl. Phys.* **2006**, *44*, 8269.

(9) Moyer, B. A.; Meyer, T. J. *J. Am. Chem. Soc.* **1978**, *100*, 3601.

(10) Gersten, S. W.; Samuels, G. J.; Meyer, T. J. *J. Am. Chem. Soc.* **1982**, *104*, 4029.

(11) Weaver, T. R.; Meyer, T. J.; Adeyemi, S. A.; Brown, G. M.; Eckberg, R. P.; Hatfield, W. E.; Johnson, E. C.; Murray, R. W.; Untereker, D. *J. Am. Chem. Soc.* **1975**, *97*, 3039.

(12) Concepcion, J. J.; Jurss, J. W.; Templeton, J. L.; Meyer, T. J. *J. Am. Chem. Soc.* **2008**, *130*, 16462.

(13) Zong, R.; Thummel, R. P. *J. Am. Chem. Soc.* **2005**, *127*, 12802.

(14) Concepcion, J. J.; Jurss, J. W.; Brennaman, M. K.; Hoertz, P. G.; Patrocinio, A. O. T.; Murakami Iha, N. Y.; Templeton, J. L.; Meyer, T. J. *Acc. Chem. Res.* **2009**, *42*, 1954.

(15) Hagfeldt, A.; Boschloo, G.; Sun, L.; Kloo, L.; Pettersson, H. *Chem. Rev.* **2010**, *110*, 6595.

(16) Wang, L.; Ashford, D. L.; Thompson, D. W.; Meyer, T. J.; Papanikolas, J. M. *J. Phys. Chem. C* **2013**, *117*, 24250.

(17) Stalder, R.; Xie, D.; Zhou, R.; Xue, J.; Reynolds, J. R.; Schanze, K. S. *Chem. Mater.* **2012**, *24*, 3143.

(18) Wasylenko, D. J.; Ganesamoorthy, C.; Koivisto, B. D.; Henderson, M. A; Berlinguette, C. P. *Inorg. Chem.* **2010**, *49*, 2202.